1 Title Page

2 Recent acceleration in coastal cliff retreat rates on the south coast of Great Britain.

3 Short Title

4 Acceleration in cliff retreat

5 Classification

6 Physical Sciences; Earth, Atmospheric and Planetary Sciences.

7 Author Affiliations

8 Martin D. Hurst[1,2], Dylan H. Rood[3], Michael A. Ellis[2], Robert S. Anderson[4], Uwe Dornbusch[5]

9 [1]School of Geographical and Earth Sciences, University of Glasgow, Glasgow, G12 8QQ, UK

10 [2]British Geological Survey, Nicker Hill, Keyworth, Nottinghamshire NG12 5GG, UK

11 [3]Department of Earth Science and Engineering, Imperial College London, South Kensington
12 Campus, London SW7 2AZ, UK

13 [4]Institute of Arctic and Alpine Research (INSTAAR) and Department of Geological Sciences,
14 University of Colorado, Boulder, CO, 80303, USA

15 [5]Environment Agency, Worthing BN11 1LD, UK

16 Corresponding author

17 Martin D. Hurst

18 School of Geographical and Earth Science

19 University of Glasgow

20 Glasgow

21 UK,

22 G12 8QQ

23 Telephone: +44 (0) 141 330 2326

24 Email: Martin.Hurst@glasgow.ac.uk

25 Keywords

26 Coastal Geomorphology, Coastal Evolution, Coastal Erosion, Rocky Coasts, Cosmogenic
27 Radionuclides

Abstract

Rising sea levels and increased storminess are expected to accelerate the erosion of soft-cliff coastlines, threatening coastal infrastructure and livelihoods. In order to develop predictive models of future coastal change, we need fundamentally to know how rapidly coasts have been eroding in the past, and to understand the driving mechanisms of coastal change. Direct observations of cliff retreat rarely extend beyond 150 years, during which humans have significantly modified the coastal system. Cliff retreat rates are unknown in prior centuries and millennia. In this study, we derived retreat rates of chalk cliffs on the south coast of Great Britain over millennial timescales by coupling high-precision cosmogenic radionuclide geochronology and rigorous numerical modelling. Measured ^{10}Be concentrations on rocky coastal platforms were compared with simulations of coastal evolution using a Monte Carlo approach to determine the most likely history of cliff retreat. The ^{10}Be concentrations are consistent with retreat rates of chalk cliffs that were relatively slow (2-6 cm yr^{-1}) until a few hundred years ago. Historical observations reveal that retreat rates have subsequently accelerated by an order-of-magnitude (22-32 cm yr^{-1}). We suggest that this acceleration is the result of reduced sediment supply that has allowed thinning of cliff-front beaches, exacerbated by both periods of increased regional storminess and anthropogenic modification of the coast.

Significance Statement

Cliffed, rocky shorelines erode when energetic waves impact on the coast. Coastal cliff retreat threatens coastal and clifftop assets and livelihoods. Understanding causes and rates of past erosion is vital to quantifying these risks, particularly when confronted with expected increases in storminess and sea-level rise, and given continued human occupation and engineering of coastal regions. Historical observations of cliff retreat span at most the last 150 years. We derived past cliff retreat rates over millennial timescales for chalk cliffs on the south coast of Great Britain by interpreting measured cosmogenic nuclides with numerical models. Our results provide evidence for accelerated erosion in recent centuries which we suggest is driven by reduced sediment supply and thinning of beaches in the face of environmental and anthropogenic changes.

Introduction

Rocky coasts are “erosional environments which form as a result of the landward retreat of bedrock at the shoreline” (1). They leave scant evidence of any previous state, making it difficult to interpret their history. Cliff retreat is driven by a combination of wave-driven cliff base erosion, subaerial weathering, and mass wasting processes, whose efficiencies are dependent on lithology

and climate. Sediment generated through mass wasting processes such as abrasion, plucking, landslides and rock-falls tends to be rapidly reworked and transported away by waves and currents, particularly for softer rock types.

The retreat of sea cliffs due to mass wasting processes threatens human livelihoods and both public and private clifftop infrastructure and development; quantitative estimates of the rate of cliff retreat are necessary to assess the associated risk. Rising sea levels and increased storminess may lead to accelerated coastal erosion rates in the future, potentially increasing hazard exposure (2–5). In order to accurately assess and predict coastal hazard in the face of future climate and land-use changes, it is necessary to understand the dynamics of cliff erosion over length and time scales relevant to the suite of processes that drive changes. In order to establish the context for modern change, we must quantify the natural variability and the long-term behavior of cliff retreat. Historical records are too short to allow us to do this: they typically span no longer than ~150 years (6, 7), which can be less than the characteristic return period of significant coastal failures (8), and they coincide with the period over which humans have significantly modified the coast. It is therefore vital that we obtain longer, reliable records of coastal change to compare with historical observations in order to understand how coastal erosion may have changed through time, what the drivers are, and how coasts may continue to evolve into the future (5).

Measurement of *in-situ* concentrations of cosmogenic radionuclides (CRNs) provide a versatile geochronometer for geomorphic studies, which facilitates dating of surface exposure and the deposition and burial of sediments, and estimation of weathering and erosion rates (9). The technique has recently been applied to rocky coasts to estimate rates of cliff retreat (10, 11) and to understand the Quaternary history of exposure, inheritance and reoccupation of shore platforms (12). Here we report a long-term record of cliff retreat in the relatively soft chalk cliffs of East Sussex, UK, which have been observed to be eroding at rates of 10-80 cm yr^{-1} over the last 150 years (7). Our long-term record was generated by coupling high-precision measurement of concentrations of ^{10}Be on a coastal platform with a numerical and statistical model that inverts these data for rates of cliff retreat at millennial timescales.

The model assumes that the coastal profile evolves through equilibrium retreat such that cliff height, platform gradient and beach width are constant through time (Fig. 1a). In nature, stable beaches play an important role in mediating cliff erosion by providing protective cover to dissipate wave energy; however, mobile beaches may provide abrasive tools to erode the cliff toe (13). Beach cover on a shore platform will also shield the platform, at least in part, from the incoming cosmic ray flux that produces ^{10}Be (10). The model presented here assumes beach width and cover is constant through time, and of sufficient thickness to completely shield the underlying platform from the production of ^{10}Be. As the cliff recedes, the rocky platform is

exposed to the production of ^{10}Be. Exposure is mediated, however, by a number of variables, including the rate of cliff retreat and the cover of water (10–12). The local water depth is dictated by tides, relative sea-level history and vertical down-wearing of the platform. This generates a theoretical 'humped' pattern of ^{10}Be concentration with distance offshore (10). We extend this model to account for beach cover, the intrinsic variability of ^{10}Be production (14), the influence of cliff height (topographic shielding) (15), and use an established glacial isostatic adjustment model (16) to provide relative sea-level history for the past 7000 years covered by the simulations. We develop a rigorous statistical analysis to compare the resulting predictions with measured ^{10}Be concentrations in order to generate quantitative estimates of cliff retreat histories (Fig. 1b) (see *Materials and Methods* section for a full description of the numerical and statistical model).

We interrogate the erosion of the Cretaceous chalk cliffs in East Sussex, UK (Fig. 2), where cliff retreat has generated wide coastal platforms characterized by abundant bands of chemically inert and erosionally resistant flint (Fig. 2a and 2b). Both the lithology and structure of the chalk are relatively uniform along the examined section of the coast, although there are known subtle variations in jointing pattern, in the orientation of gentle fold axes, and the associated dip of sub-horizontal bedding of the chalk and flint bands (17). Our modeling assumes that the geological properties of the cliff and platform have been constant as retreat has occurred. Waves approach predominantly from the open Atlantic Ocean into the relatively narrow English Channel (Fig. 2c). Previous studies suggest the wave directions have been consistent during the mid-late Holocene (18), although storminess may have varied (19, 20). The coastline is managed as part of the South Downs National Park and is designated a Site of Special Scientific Interest, a Marine Conservation Zone, an Area of Outstanding Natural Beauty and a Heritage Coast by the UK government. There has been little direct human intervention; the chalk cliffs therefore evolve without any attempts to control erosion (21).

Chalk cliff heights range from 12 m near Cuckmere Haven up to 150 m at Beachy Head. The cliffs are near vertical along the length of the coastline and are connected to a low gradient rock platform extending several hundred meters offshore (Fig. 2d, 2e). At the junction between cliff and platform there are intermittent fringing beaches composed of flint pebbles and cobbles mixed with sand. These are known to have been more continuous and of larger volume during the 19th century (7). Frequent cliff failures result in aprons of chalk debris that are subsequently reworked by wave action. A variety of cliff failure mechanisms have been observed, including vertical collapses, wedge collapses, rockfalls, rotational failures and toppling (17); all of these processes can result in several meters of clifftop retreat in a single event. Erosion of platforms appears to

129 occur through a combination of vertical downwearing due to frost action, mechanical and
130 biological abrasion (22), and sub-horizontal step retreat (23).

131 Mapped clifftop positions from 1873-2001 historical maps and aerial photographs reveal that cliff
132 retreat rates vary between 0.05 and 0.8 m y^{-1} (Fig. 2c) (7). Extrapolating this range of historical
133 retreat rates back in time, a ~350 m platform (widest observed sub-aerially exposed platform at
134 the study site) can form in between 450 and 7000 years, and therefore certainly within the
135 Holocene. The model and CRN data presented here allowed us to constrain more precisely the
136 platform age and cliff retreat rates.

137 Samples of *in situ* flint exposed on the rock platform were collected along transects roughly
138 perpendicular to the cliff face at Hope Gap (HG; Fig. 2d) and Beachy Head (BH; Fig. 2e) at low tides
139 during spring tides 24th-25th July 2013. Cliff heights at HG and BH are 15 m and 50 m, respectively.
140 These transects were chosen to maximize platform width (minimizing platform gradient) in
141 order to sample as far offshore as possible. We collected samples from local topographic highs on
142 sections of the platform away from areas that exhibited significant roughness due to runneling or
143 block removal (Fig 3). Distance to a fixed position on the cliff and the height of the cliff were
144 measured with a laser range finder. In addition, we sampled rock from inside a sea cave near to
145 HG to estimate inherited ^{10}Be concentration prior to platform exposure.

146 ^{10}Be sample preparation was carried out at the Scottish Universities Environmental Research
147 Centre (SUERC) using isotope dilution chemistry. ^{10}Be/^{9}Be analyses by Accelerator Mass
148 Spectrometry (AMS) were conducted at Lawrence Livermore National Laboratory (LLNL) to
149 determine ^{10}Be concentrations (see Methods section for full details of chemistry and AMS
150 measurements).

151 In order to interpret Holocene cliff retreat rate, we compared the measured distributions of ^{10}Be
152 concentrations across the coastal platform to predicted concentrations from numerical modeling
153 of coastal retreat and ^{10}Be accumulation. We searched for the most likely cliff retreat rate
154 histories by comparing observed ^{10}Be concentrations to modeling results via maximum likelihood
155 estimation (MLE) using Markov Chain Monte Carlo (MCMC) (24) ensembles (each with 200k
156 iterations). We modeled three possible scenarios for the history of cliff retreat: (i) steady rate of
157 cliff retreat for the entire Holocene; (ii) linear change in erosion rate throughout the Holocene
158 (either acceleration or deceleration); (iii) step change in erosion rate at an unknown time
159 (acceleration or deceleration). The presence of a beach was incorporated assuming that no ^{10}Be
160 production occurs beneath the beach, i.e. that the beach thickness is sufficient to diminish ^{10}Be
161 production entirely. Beach width was treated as a free parameter in the MCMC procedure, but is
162 held constant throughout any single cliff retreat model run, as there is little information about

beach width change during the Holocene. Estimates and confidence intervals of cliff retreat rates and beach width for each scenario were obtained from the MCMC-derived posterior probability distributions as the median and 95% confidence limits (see Supplementary Materials).

Results

Broadly, concentrations of ^{10}Be across the coastal transects show a "humped" profile (10) (Fig. 4a and 4b). One sample (HG-12) showed anomalously high ^{10}Be concentration and we therefore treated it as an outlier. Despite taking care to sample only *in-situ* flint nodules, it is possible that this HG-12 sample was not *in-situ* and had been transported for a significant period at the surface, allowing high exposure to cosmic rays. We collected sample HG-15 from an inward-directed face 8 m deep inside a cave in the 30 m high cliff, adjacent to the HG transect (Fig. 3a). This sample contained an appreciable concentration of ^{10}Be, suggesting that any newly exposed platform may contain an inherited contribution of ^{10}Be (up to 30-50% of the measured concentrations). This inherited contribution is likely due to production by the deep penetration of the energetic muons (25) into the landscape. The inherited concentration measured here is similar to concentrations measured on a similar platform at Mesnil-Val on the opposite side of the English Channel (10). This highlights that future CRN studies on coastal platforms should be careful to assess potential inheritance or risk significantly underestimating retreat rates. We modeled the production of muogenic ^{10}Be as a function of depth and surface lowering rates (26) (see *Materials and Methods*) to compare with the measured inherited ^{10}Be concentrations (Fig. 5). We plot the depth of the measured concentrations as the cliff height, and these concentrations are consistent with muogenic production for slow surface lowering rates in the range 0.01-0.04 mm yr^{-1}.

Prior to the MCMC inversion employed to determine most likely retreat scenario and rates, we corrected concentrations for inherited ^{10}Be using the measured concentrations at both HG-15 and BH-13 for the HG and BH transects, respectively (shaded grey area labelled 'inheritance' in Figs. 4a and 4b). Note also that site HG-10 was sampled twice (HG-10a and HG-10b), i.e. from two different adjacent flint nodules on the rock platform. The concentrations returned from these two were within measurement error of one another (see Fig. 4a, Table S1).

The most likely retreat scenarios were determined by MLE using MCMC ensembles, resulting in likelihood-weighted probability distributions (Fig. 6; see also supplementary materials). At both transects the best fit scenario included a recent step change in retreat rate, with a reduction from 5.7 (+0.3/-0.3) to 1.3 (+1.1/-0.3) cm yr^{-1}, 308 (+135/-100) years ago at Hope Gap (Fig. 6); and an increase in retreat rate from 2.6 (+0.2/-0.2) to 30.4 (+8.3/-106.) cm yr^{-1}, 293 (+170/-80) years ago at Beachy Head (see also Table S2 and S3 in Supplementary Materials). However, both sites

have experienced a recent acceleration in erosion rates as evidenced by observed rates of ~32 cm yr^{-1} and ~22 cm yr^{-1} since 1870 at Hope Gap and Beachy Head, respectively (7).

Discussion

To date, application of CRNs to quantify long-term coastal process rates have been few (10–12), but these techniques provide a new opportunity to integrate annual to decadal observations with long-term rates and antecedent coastal conditions. Observed rates of cliff retreat at Hope Gap (~32 cm yr^{-1}) and Beachy Head (~22 cm yr^{-1}) imply that the 250-350 m width of platform that we have sampled is young, forming in the last 1500 years. Such recent retreat and young platform age would result in negligible ^{10}Be accumulation on the platform, which is inconsistent with the measured ^{10}Be concentrations. Thus, the rates suggested by historical observations cannot be extrapolated back in time; instead, cliff retreat rates must have recently accelerated to their observed values.

^{10}Be concentrations at Hope Gap demonstrate that slower cliff retreat (~5.7 cm yr^{-1}) persisted for much of the Holocene and do not match the historically observed higher rates (Fig. 4a). On the contrary, our modeling results suggest a recent slowdown to ~1.3 cm yr^{-1} over the last 300 years. This slowdown is principally allowing better fit to HG-13 and HG-14, the samples nearest the cliff. These sites may have elevated ^{10}Be concentrations due to minimal platform downwear in this zone, sampled at ~ 1 m elevation above mean sea level in the upper intertidal zone (Fig. 3a). Nevertheless, the most landward platform sample (HG-14) is 50 m from the modern cliff; at 32 cm yr^{-1} (the observed retreat rate since 1870s), this 50 m would have occurred in the last 156 years. Hence, we may not have sampled close enough to the cliff to detect an acceleration in cliff retreat rates that must have occurred during this time. Future sampling at this site could focus on higher resolution sampling nearer the cliff to resolve the historical signal.

Measured ^{10}Be concentrations at Beachy Head indicate long-term average retreat rates that are much slower than historical rates for most of the Holocene. In contrast with nearshore samples at Hope Gap, low concentrations in the nearshore region of Beachy Head are consistent with recent, rapid retreat, as corroborated by historical observations. Low concentrations persist to 145 m out from the modern cliff (Fig. 4b); at historical retreat rates of 22 cm yr^{-1} this cliff would have retreated 145 m in the last 650 years, implying acceleration must have occurred within this timeframe. Our modeling results suggest a significant increase in retreat rates in the last 200-500 years. The large uncertainty estimates with respect to the timing of this change result from a tradeoff between the timing of acceleration in retreat rates and the increased retreat rate itself. More rapid retreat rates require the acceleration to have occurred more recently to expose the 145 m of platform with consistently low ^{10}Be concentrations.

At both sites, ^{10}Be concentrations demonstrate that cliff retreat was slow for much of the Holocene, which contrasts with substantially higher historical rates of cliff retreat. Thus, we conclude that the coast of East Sussex, previously a relatively stable, slowly eroding coastline, has undergone a recent increase in rates of cliff retreat.

We assume that equilibrium retreat is an appropriate model for the morphological evolution of the studied shorelines. Alternative morphological models include shore platforms that are widening and shallowing through time, which tends to cause deceleration in cliff retreat rates due to increased wave energy dissipation (27, 28). The platforms we have studied, however, are relatively steep (gradient 1:60 m; Fig. 3), suggesting that equilibrium retreat is appropriate over the millennial timescales studied. Moreover, our modeling concludes that platforms that were widening and shallowing through time will result in distributions of ^{10}Be concentrations that are distinct from those predicted under the equilibrium retreat assumption (29); however, the distribution of concentrations measured in the shore platforms for this study are consistent with equilibrium retreat. Nevertheless, differences in lithological resistance or susceptibility perhaps related to jointing (17) between our two studied transects may account for the 45% differences in retreat rates, with Hope Gap recording more rapid retreat over both long timescales as revealed by ^{10}Be concentrations, and historical timescales, compared to the equivalent time periods at Beachy Head.

In addition, our modeling assumes that beach width has not changed during the Holocene. If beach widths had in fact been wider and thicker in the mid-late Holocene, less ^{10}Be would have accumulated on the coastal platform because the platform would have been shielded by sedimentary cover (11). The influence of additional cover would require even slower long-term retreat rates to match the observed ^{10}Be concentrations, and would increase the difference between long-term and historic cliff retreat rates. Beaches play a dual role in affecting cliff erosion: they provide the abrasive tools to achieve erosion, but also provide protective cover to dissipate wave energy before it reaches the cliff toe (13, 30). Our modeling demonstrates that the presence or absence, and variability of beach cover exerts only minor control on the distribution of ^{10}Be across the shore platform (29). If beaches were wider and thicker in the past, then measured ^{10}Be concentrations would be lower than if no beaches were present; lower concentrations would suggest faster apparent erosion rates than had actually occurred. In this sense, our estimates of long-term cliff retreat rates may be maxima.

Acceleration of chalk cliff erosion is likely related to an increase in wave energy delivered to the cliff face, and we offer two potential explanations for this increase. The first is related to climate change during the Little Ice Age (LIA, ~600-150 years BP). A growing body of proxy-based evidence supports increased storminess in the north Atlantic c. 600-250 years BP (19) associated

with the negative phase of the North Atlantic Oscillation that resulted in a drier, colder climate in northern Europe (20). General circulation climate model simulations have shown that during the LIA, the paths and the intensity of cyclones, and associated extremes of precipitation and wind speed, may have shifted southward below 50°N. Such conditions may have increased the delivery of wave energy to the coast due to both the number of energetic events and their severity. The second explanation is related to the availability and role of beach sediment. Sediment protects the platform against vertical downwearing and serves to dissipate wave energy otherwise available to drive cliff erosion. Beaches within the study area are known to have been thinning during the Holocene (7), in part supplying the wider beaches to the east (down-drift) (31–33).

Sediment supply to the beaches may also be related to human intervention at the coast. While there are no active interventions protecting the studied coastline, engineering activities since the late-19th century, designed to protect several km of the coastline 2-15 km to the west (updrift), have reduced the supply of littoral sediment along the studied coastline; beach widths have been observed to be declining or been lost along the length East Sussex coastline (7). Numerical modeling has demonstrated that shoreline interventions can result in significant non-local impact many km down-drift from the protected sites (3, 34).

Our methods do not allow us to attribute the recent acceleration in cliff retreat rates in East Sussex to anthropogenic activity, to a response to progressive thinning of beach material or to increased storminess during the LIA. However, these results would suggest that beaches play an important role in regulating coastal erosion along the East Sussex coast of southern Great Britain. The dynamics and fate of beaches on shore platforms and how they link to long-term coastal evolution remains an outstanding research area within coastal geomorphology (35).

Conclusions

Efforts to forecast future coastal change at rocky coasts in the face of rising sea level and increased storminess require detailed understanding of past rates of cliff retreat in response to environmental conditions over long timescales. Cosmogenic radionuclide samples from coastal platforms that are a common coastal landform globally offer a promising approach to obtaining such records (35). Here, cosmogenic ^{10}Be concentrations from two shore platforms on the coast of East Sussex in southern Great Britain reveal that retreat rates between 2-6 cm yr^{-1} prevailed for most of the Holocene, and contrast dramatically with historical records of rapid retreat at 22-32 cm yr^{-1} at the same sites during the last 150 years (7). Our measurements demonstrate that acquisition of long-term records of coastal change can reveal marked changes in coastal dynamics in the relatively recent past. At our study site, these changes likely reflect beach dynamics that has led to thinning of beach sediment, which in turn has increased cliff retreat rates.

Materials and Methods

Sample preparation and analysis

We processed samples at SUERC according to modified protocols developed for this study. We crushed and sieved flint nodule samples to 0.25-0.50 mm size fraction and performed magnetic separation to remove magnetically susceptible particles.

To purify flint (amorphous SiO_2 with the same chemical formula as quartz, but a different structure) and remove atmospherically derived ^{10}Be adhered to the outer parts of the grains (36), each sample was washed and leached in sub-boiling 2% nitric acid. Samples were dried and etched in 35% hexaflorosilicic acid, followed by repeated 16% hydrofluoric acid etches. The samples were then dried and aliquots assayed to determine their elemental abundances by ICP-OES. Samples contained high levels of impurities, including Al, Ca, Na, K, Mg, Ti, and/or Fe, and were additionally etched; upon re-assay, elemental concentrations remained constant, and we therefore judged that observed concentrations were inherent to the flint material.

Samples were transferred to a cleanroom, rinsed in 18.2 MΩ water and dried. Samples were then massed (~50-60 g of flint) and ~200 µg low-background beryl-derived Be carrier was added by mass. The samples were dissolved in sub-boiling hydrofluoric acid. The hydrofluoric acid was evaporated and the resulting digestion cakes were fumed to dryness at least 3 times to convert to chloride form, then taken up in hydrochloric acid (37). Insoluble residues were removed by centrifugation. In order to reduce the high concentrations of cations and anions in the solution, samples were first precipitated at pH8 as hydroxides (38). Post-precipitation, ~30 mg of anions and cations were still present in each sample. Because the vast majority of the ions in solution were cations, the samples were passed though anion exchange columns using 2 ml of AG 1-X8 (200-400 dry mesh) resin to remove iron, using standard protocols. After conversion to sulfate form with sulfuric acid, samples were passed through large (20 ml) cation exchange AG 50W-X8 (20-50 dry mesh size) resin columns to remove impurities (39), including Ti, Al, and B, and to isolate Be. Elution curves for these large columns with high cation loads were developed prior to sample processing and milliequivalent (meq) calculations were made for each sample based on post-precipitation ICP-OES data to ensure that cation loads were at or below ~50% of the available column capacity. After cation elution, yield test samples were collected from the Be fractions to determine their purity and to ensure that sufficient material was available for high quality isotopic analyses; Be fractions from large columns were ~75% (~150 µg) with a few 100 µg of each of Al, Mg, and K. Nearly all of the missing Be was lost during the first pH8 hydroxide precipitation, rather than during subsequent ion exchange chromatography. To further purify the Be fractions, these solutions were dried down, dissolved in sulfuric acid, and passed through an

additional 2 ml cation column using standard procedures (as above, but using an elution curve for the smaller columns). After the second cation column, Be fractions were free of impurities and no additional Be was lost during the second elution.

The final Be fractions were precipitated at pH8 as hydroxides, centrifuged, washed with 18.2 MΩ water, centrifuged, decanted, and dried. The dried material was ignited in a furnace to convert to Be oxide, mixed with Nb in a 1:1 molar ratio and packed into stainless steel cathodes for isotopic analysis at LLNL by AMS (40).

At the LLNL AMS facility, each cathode was measured at least three times. Initial sample $^{9}Be^{3+}$ beam currents averaged ~18 uA, ~75% of standard cathodes. The data were normalized to the 07KNSTD3110 standard with a reported $^{10}Be/^{9}Be$ ratio of 2.85×10^{-12}, which is consistent with the revised ^{10}Be decay constant (41). Secondary standards produced by K. Nishiizumi were run as unknowns to confirm the linearity of the isotopic measurements.

Two full-process blanks (Be carrier only) were processed with each batch of samples. The average measured blank isotopic ratio for each batch was subtracted from the measured isotopic ratios of the samples in that batch with uncertainties (i.e. standard deviation samples and blanks) propagated in quadrature (see Table S1). The $^{10}Be/^{9}Be$ blank ratios for 2 blanks run with the samples in one batch (HG samples) averaged $2.1\pm0.07\times10^{-15}$, whereas 2 blanks in the second batch (BH samples) averaged $6.3\pm2.0\times10^{-15}$, both representing a relatively small portion (~3-11% and ~11-35%, respectively) of the measured sample isotopic ratios of samples in each batch.

Modeling ^{10}Be Production

The concentration of ^{10}Be in rock, N (atoms g^{-1}), at depth below the rock platform surface, z, (m) evolves through time, t, according to (29):

$$\frac{dN}{dt} = \sum_i S_T S_G S_W P_i e^{-(z/z_i^*)} - \lambda N$$

Here the first term on the right hand side reflects production of radionuclides, and the second term their decay. The subscript i refers to different production pathways; for ^{10}Be this is dominated by spallation (26), with a minor contribution from muogenic production. Production due to muons is modelled with a single exponential term (25). S_T is a topographic shielding scaling factor that adjusts the incoming cosmic ray flux depending on the proportion of the sky blocked by the presence of the cliff, and is modelled following established procedures (15). S_T varies with distance from the cliff, and the model assumes a vertical cliff of constant height in space and time. S_G is a scaling factor reflecting temporal variation in incoming cosmic ray flux due to solar activity and deviation in the strength of Earth's magnetic field, calculated following Lifton et al. (14). S_W

is a scaling factor reflecting shielding of the platform due to water cover, averaged over a single tidal cycle, calculated following Regard et al. (10). We used a glacio-isostatic adjustment model for the UK to predict relative sea level change at the field sites (16). P_i is the surface production rate specific to the production pathway. For spallation, the value of P = 4.008 at g^{-1} yr^{-1} was obtained for the field site from the Lifton et al. (14) scaling scheme. For muogenic production a single median value of P = 0.028 at g^{-1} yr^{-1} was used to integrate both fast muon interactions and negative muon capture reactions (25). $z_i^* = \rho_r/\Lambda_i$ is a production pathway-specific attenuation length scale, where ρ_r is rock density (1800 kg/m^3 used here for chalk) (17) and Λ_i is the attenuation factor. For spallation, Λ = 1600 kg m^{-2} was used, and Λ = 42000 kg m^{-2} was used for muogenic production. $\lambda = 4.99 \times 10^{-7}$ is the ^{10}Be radioactive decay constant (42, 43).

Prediction of the expected ^{10}Be concentration inherited (Fig. 5) due to deep penetration of energetic muons N_μ (atoms g^{-1}), where the subscript μ refers to the muogenic production pathway, were calculated assuming steady-state surface lowering rate ε (mm yr^{-1}) (26) according to:

$$N_\mu(z) = \frac{P_\mu}{\lambda + \varepsilon / z_\mu^*} e^{-(z/z_\mu^*)}$$

Determining Retreat History

In order to find the retreat rate histories that best replicate the observed ^{10}Be concentrations, we performed a Markov Chain Monte Carlo (MCMC) analysis (24) to produce posterior probability density functions for cliff retreat rates (similar to Hurst et al. (44)). A Metropolis-Hastings algorithm was used to vary parameters (45). We calculate and maximize the likelihood L for a given set of parameters:

$$L = \prod_{j=1}^{n} \frac{1}{\sqrt{2\pi}\sigma_j} \exp\left[-\frac{\left(N_j^{meas} - N_j^{\mathrm{mod}}\right)^2}{2\sigma_j^{\,2}} \right]$$

where n is the number of observations of ^{10}Be concentration N, the superscripts ^{meas} and ^{mod} refer to corresponding measured and modelled ^{10}Be concentrations, and σ is the confidence range of measured ^{10}Be concentrations.

Three scenarios of cliff retreat were run for comparison with measured ^{10}Be concentrations: i) A single retreat rate ε_1 applied through the entire Holocene; ii) A step change in retreat rate from ε_1 to ε_2 at time t; iii) A gradual change in retreat rate from ε_1 to ε_2 throughout the Holocene (7 ka BP to present). A fixed beach width W was assumed throughout each model run. After each run in the MCMC, new values for ε_1, ε_2, t and W were randomly selected from a Gaussian probability

distribution centered on the previous accepted values, with standard deviations tailored to a target acceptance rate of 23% (46). The likelihood of each iteration is compared to that of the last accepted parameter set such that if the ratio of the current to the last accepted iteration >1 then the new parameter set is accepted. If the ratio <1, then the new parameters may be accepted with a probability of acceptance equal to the likelihood ratio (to allow the chain to fully explore the parameter space). The "burn in" period was less than 1000 iterations in all cases, and each MCMC was run for 200k iterations (45). The posterior probability distribution of each parameter was generated as a likelihood-weighted frequency distribution from the Markov Chain iterations. Parameter values and confidence intervals were then determined as the median and 95% limits on the probability distribution (see supplementary materials for plots).

Acknowledgements

We thank Matthew Booth, Peter Hopson and Katie Whitbread for assistance in the field, and Maria Miguens-Rodriguez and Victoria Forbes for assistance with sample preparation in the laboratory. We are grateful to the staff of the Center for Accelerator Mass Spectrometry at Lawrence Livermore National Laboratory for support during $^{10}Be/^{9}Be$ measurements. Andrew Barkwith, Claire Mellett and Hilary Gasman-Deal provided helpful reviews and editorial assistance on an early version of the paper. This paper is published with the permission of the Executive Director of the British Geological Survey and was supported in part by the Climate and Landscape Change research programme at the BGS. R.S.A. acknowledges support from NSF grant EAR-1552883, EAR-0724960 and EAR-1331828.

References

1. Kennedy DM, Stephenson WJ, Naylor L a. (2014) Chapter 1 Introduction to the rock coasts of the world. *Geol Soc London, Mem* 40(1):1–5.

2. Barkwith A, Thomas CW, Limber PW, Ellis MA, Murray AB (2014) Coastal vulnerability of a pinned, soft-cliff coastline - Part I: Assessing the natural sensitivity to wave climate. *Earth Surf Dyn* 2(1):295–308.

3. Barkwith A, et al. (2014) Coastal vulnerability of a pinned, soft-cliff coastline, II: Assessing the influence of sea walls on future morphology. *Earth Surf Dyn* 2(1):233–242.

4. Ashton AD, Walkden MJA, Dickson ME (2011) Equilibrium responses of cliffed coasts to changes in the rate of sea level rise. *Mar Geol* 284(1-4):217–229.

5. Trenhaile AS (2014) Climate change and its impact on rock coasts. *Geol Soc London, Mem* 40(1):7–17.

6. Brooks SM, Spencer T (2010) Temporal and spatial variations in recession rates and sediment release from soft rock cliffs, Suffolk coast, UK. *Geomorphology* 124(1-2):26–41.

7. Dornbusch U, Robinson DA, Moses CA, Williams RBG (2008) Temporal and spatial variations of chalk cliff retreat in East Sussex, 1873 to 2001. *Mar Geol* 249(3-4):271–282.

8. Recorbet F, et al. (2010) Evidence for active retreat of a coastal cliff between 3.5 and 12 ka in Cassis (South East France). *Geomorphology* 115(1-2):1–10.

9. Granger DE, Lifton NA, Willenbring JK (2013) A cosmic trip: 25 years of cosmogenic nuclides in geology. *Bull Geol Soc Am* 125(9-10):1379–1402.

10. Regard V, et al. (2012) Late Holocene seacliff retreat recorded by 10Be profiles across a coastal platform: Theory and example from the English Channel. *Quat Geochronol* 11:87–97.

11. Rogers HE, Swanson TW, Stone JO (2012) Long-term shoreline retreat rates on Whidbey Island, Washington, USA. *Quat Res* 78(2):315–322.

12. Choi KH, Seong YB, Jung PM, Lee SY (2012) Using Cosmogenic 10 Be Dating to Unravel the Antiquity of a Rocky Shore Platform on the West Coast of Korea. *J Coast Res* 282(3):641–657.

13. Sunamura T (1982) A wave tank experiment on the erosional mechanism at a cliff base. *Earth Surf Process Landforms* 7:333–343.

14. Lifton N, Sato T, Dunai TJ (2014) Scaling in situ cosmogenic nuclide production rates using analytical approximations to atmospheric cosmic-ray fluxes. *Earth Planet Sci Lett* 386:149–160.

15. Dunne J, Elmore D, Muzikar P (1999) Scaling factors for the rates of production of cosmogenic nuclides for geometric shielding and attenuation at depth on sloped surfaces. *Geomorphology* 27(1-2):3–11.

16. Bradley SL, Milne GA, Shennan I, Edwards R (2011) An improved glacial isostatic adjustment model for the British Isles. *J Quat Sci* 26(5):541–552.

17. Mortimore RN, Lawrence J, Pope D, Duperret A, Genter A (2004) Coastal cliff geohazards in weak rock: the UK Chalk cliffs of Sussex. *Geol Soc London, Eng Geol Spec Publ* 20(1):3–31.

18. Shennan I, Horton B (2002) Holocene land- and sea-level changes in Great Britain. *J Quat Sci* 17(5-6):511–526.

19. Sorrel P, et al. (2012) Persistent non-solar forcing of Holocene storm dynamics in coastal sedimentary archives. *Nat Geosci* 5(12):892–896.

20. Olsen J, Anderson NJ, Knudsen MF (2012) Variability of the North Atlantic Oscillation over the past 5,200 years. *Nat Geosci* 5(11):1–14.

21. SECG (2006) *Beachy Head to Selsey Bill Shoreline Management Plan* (South East Coastal Group) Available at: http://www.se-coastalgroup.org.uk/wp-content/uploads/2013/10/Beachy-Head-to-Selsey-Bill-SMP-FINAL.pdf.

22. Robinson DA, Jerwood LC (1987) Sub-aerial weathering of chalk shore platforms during harsh winters in southeast England. *Mar Geol* 77(1-2):1–14.

23. Dornbusch U, Robinson DA (2011) Block removal and step backwearing as erosion processes on rock shore platforms: A preliminary case study of the chalk shore platforms of south-east England. *Earth Surf Process Landforms* 36(5):661–671.

24. Hastings WK (1970) Monte Carlo sampling methods using Markov chains and their applications. *Biometrika Vol* 57(1):97–109.

25. Braucher R, et al. (2013) Determination of muon attenuation lengths in depth profiles from in situ produced cosmogenic nuclides. *Nucl Instruments Methods Phys Res Sect B Beam Interact with Mater Atoms* 294:484–490.

26. Lal D (1991) Cosmic ray labeling of erosion surfaces: in situ nuclide production rates and erosion models. *Earth Planet Sci Lett* 104:424–439.

27. Trenhaile AS (2000) Modeling the development of wave-cut shore platforms. *Mar Geol* 166(1-4):163–178.

28. Walkden MJA, Hall JW (2005) A predictive Mesoscale model of the erosion and profile development of soft rock shores. *Coast Eng* 52(6):535–563.

29. Hurst MD, Rood DH, Ellis MA (2016) Controls on the distribution of cosmogenic 10Be across shore platforms. *Earth Surf Dyn Discuss* (August):1–38.

30. Limber PW, Murray AB (2011) Beach and sea-cliff dynamics as a driver of long-term rocky coastline evolution and stability. *Geology* 39(12):1147–1150.

31. Jennings S, Smyth C (1990) Holocene evolution of the gravel coastline of East Sussex. *Proc - Geol Assoc* 101(3):213–224.

32. Nicholls RJ (1990) Holocene evolution of the gravel coastline of East Sussex: discussion. *Proc - Geol Assoc* 102(4):301–305.

33. Mellett CL, et al. (2012) Preservation of a drowned gravel barrier complex: A landscape evolution study from the north-eastern English Channel. *Mar Geol* 315-318:115–131.

34. Ells K, Murray AB (2012) Long-term, non-local coastline responses to local shoreline stabilization. *Geophys Res Lett* 39(18):1–7.

35. Naylor LA, Kennedy DM, Stephenson WJ (2014) Synthesis and conclusion to the rock coast geomorphology of the world. *Geol Soc London, Mem* 40:283–286.

36. Kohl CP, Nishiizumi K (1992) Chemical isolation of quartz for measurement of in-situ -produced cosmogenic nuclides. *Geochim Cosmochim Acta* 56(9):3583–3587.

37. Stone J (2001) *Extraction of Al and Be from quartz for iostopic analysis* Available at: http://depts.washington.edu/cosmolab/chem/Al-26_Be-10.pdf.

38. Ochs M, Ivy-Ochs S (1997) The chemical behavior of Be, Al, Fe, Ca and Mg during AMS target preparation from terrestrial silicates modeled with chemical speciation calculations. *Nucl Instruments Methods Phys Res Sect B Beam Interact with Mater Atoms* 123(1-4):235–240.

39. Ditchburn RG, Whitehead NE (1994) The separation of 10Be from silicates. *3rd Work South Pacific Environ Radioact Assoc*:4–7.

40. Rood DH, Hall S, Guilderson TP, Finkel RC, Brown TA (2010) Challenges and opportunities in high-precision Be-10 measurements at CAMS. *Nucl Instruments Methods Phys Res Sect B Beam Interact with Mater Atoms* 268(7-8):730–732.

41. Nishiizumi K, et al. (2007) Absolute calibration of 10Be AMS standards. *Nucl Instruments Methods Phys Res Sect B Beam Interact with Mater Atoms* 258(2):403–413.

42. Korschinek G, et al. (2010) A new value for the half-life of 10Be by Heavy-Ion Elastic Recoil Detection and liquid scintillation counting. *Nucl Instruments Methods Phys Res Sect B Beam Interact with Mater Atoms* 268(2):187–191.

43. Chmeleff J, von Blanckenburg F, Kossert K, Jakob D (2010) Determination of the 10Be half-life by multicollector ICP-MS and liquid scintillation counting. *Nucl Instruments Methods Phys Res Sect B Beam Interact with Mater Atoms* 268(2):192–199.

44. Hurst MD, Mudd SM, Attal M, Hilley G (2013) Hillslopes Record the Growth and Decay of Landscapes. *Science (80-)* 341(6148):868–871.

45. Metropolis N, Rosenbluth AW, Rosenbluth MN, Teller AH, Teller E (1953) Equation of state calculations by fast computing machines. *J Chem Phys* 21(6):1087–1092.

46. Roberts GO, Gelman A, Gilks WR (1997) Weak convergence and optimal scaling of random

walk Metropolis algorithms. *Ann Appl Probab* 7(1):110–120.

Figure Legends

Figure 1: Setup for modeling the accumulation of ^{10}Be on a coastal platform. (a) The model assumes equilibrium retreat such that as the coast evolves, the cross section morphology remains steady while translating shoreward according to the prescribed retreat rate. Beach width was held constant during each model run, and the elevation of the coastal profile tracks relative sea level change. (b) Schematic illustration of a rocky coast and platform showing the expected "humped" relationship between distance from the cliff and ^{10}Be concentration.

Figure 2: Location and observed historical cliff retreat rates. (a) Photograph of platform and Seven Sisters chalk cliffs. (b) Location map showing study area in Cretaceous Chalk in East Sussex, United Kingdom. (c) Shaded relief map derived from stitched LiDAR topography and multibeam bathymetry (data courtesy of the Channel Coast Observatory (CCO); www.channelcoast.org). Mapped 1870s and 2001 cliff lines and associated observed cliff retreat rates from are plotted along the coast after Dornbusch et al. (7). The box plot shows the 5th, 25th, 50th, 75th and 95th percentile of these historic retreat rates above the legend. The wave rose diagram shows wave conditions during 2014 with dominant wave approach from SW (data courtesy of CCO). (d) and (e) Shaded relief draped with 2008 aerial photographs (data courtesy of CCO) for field sites at (d) Hope Gap and (e) Beachy Head, respectively. Black triangles show the locations of flint samples collected for CRN analysis for use in this study. Average 20th century retreat rates are 0.32 and 0.22 m y^{-1}, respectively.

Figure 3: Swath profiles of platform morphology from stitched LiDAR and multibeam elevation data (data courtesy of the Channel Coast Observatory; www.channelcoast.org) and sample locations (black triangles) for (a) Hope Gap and (b) Beachy Head transects. Black lines are mean elevation within a 10 m wide swath, grey shaded region shows the range of elevations within the swath.

Figure 4: Measured ^{10}Be concentrations and 1σ uncertainties (open circles and whiskers respectively), and most likely retreat scenarios (colored lines and shaded regions showing median and 95% confidence interval) for (a) Hope Gap and (b) Beachy Head transects. Concentrations of ^{10}Be generally increase and then decrease offshore. The sample highlighted in red on the Hope Gap transect (a) was treated as an outlier (see Discussion in text). The minimum measured concentration in each transect was assumed to represent the inherited concentration of ^{10}Be (see text for further discussion). The most likely retreat scenarios in both cases were a

553 recent step change in retreat rate, with (a) a reduction from 5.7 (+0.3/-0.3) to 1.3 (+1.1/-0.3) cm
554 yr^{-1}, 308 (+135/-100) years ago at Hope Gap; and (b) an increase in retreat rate from 2.6 (+0.2/-
555 0.2) to 30.4 (+8.3/-106.) cm yr^{-1}, 293 (+170/-80) years ago at Beachy Head.

556 Figure 5: Steady-state ^{10}Be concentrations as a function of depth generated by deep-penetrating
557 muons for surface lowering rates of up to 0.1 mm yr^{-1}. Red symbols show measured inherited
558 concentrations with depth taken as the local cliff height for each site. Measured inheritance is
559 consistent with surface lowering rates of 0.01-0.04 mm yr^{-1}.

560 Figure 6: Example probability density (top row) and cumulative probability (bottom row) of the
561 two retreat rates, the timing of change, and beach width for the step-change scenario MCMC
562 ensemble at Hope Gap. Values and uncertainties were taken as the median (solid line) and 95%
563 confidence range (dashed lines and grey shading) from the cumulative density plots on the
564 bottom row.

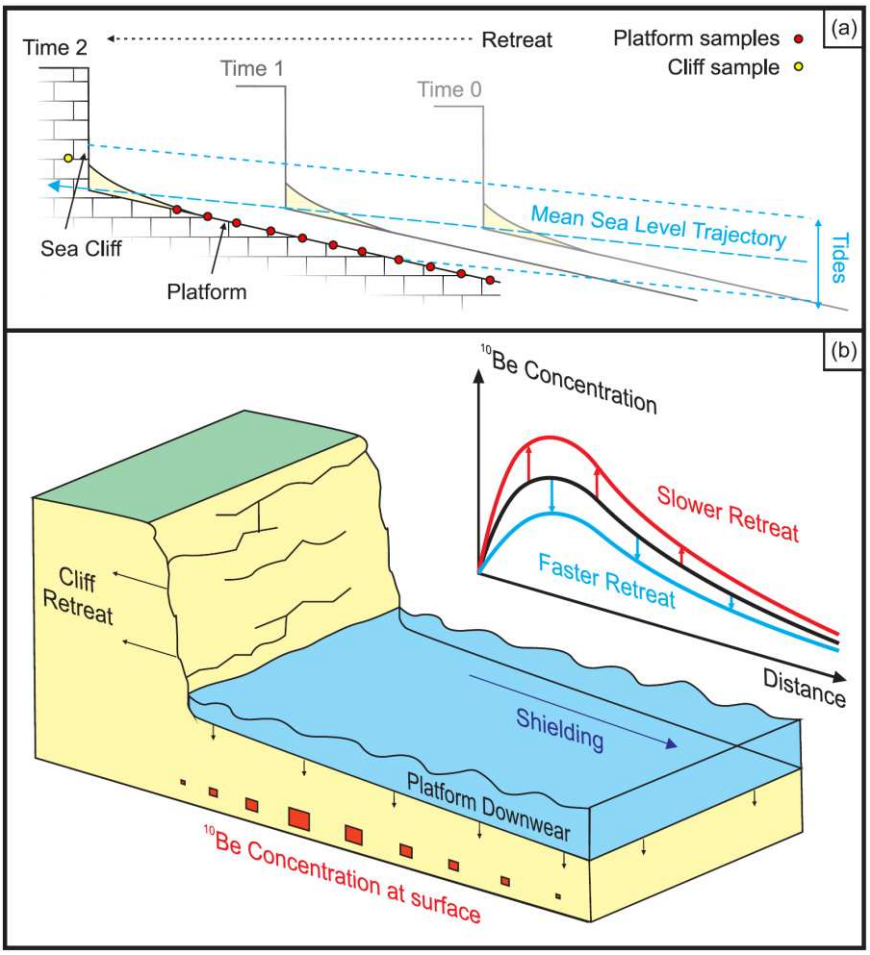

Figure 1: Setup for modeling the accumulation of ^{10}Be on a coastal platform. (a) The model assumes equilibrium retreat such that as the coast evolves, the cross section morphology remains steady while translating shoreward according to the prescribed retreat rate. Beach width was held constant during each model run, and the elevation of the coastal profile tracks relative sea level change. (b) Schematic illustration of a rocky coast and platform showing the expected "humped" relationship between distance from the cliff and ^{10}Be concentration.

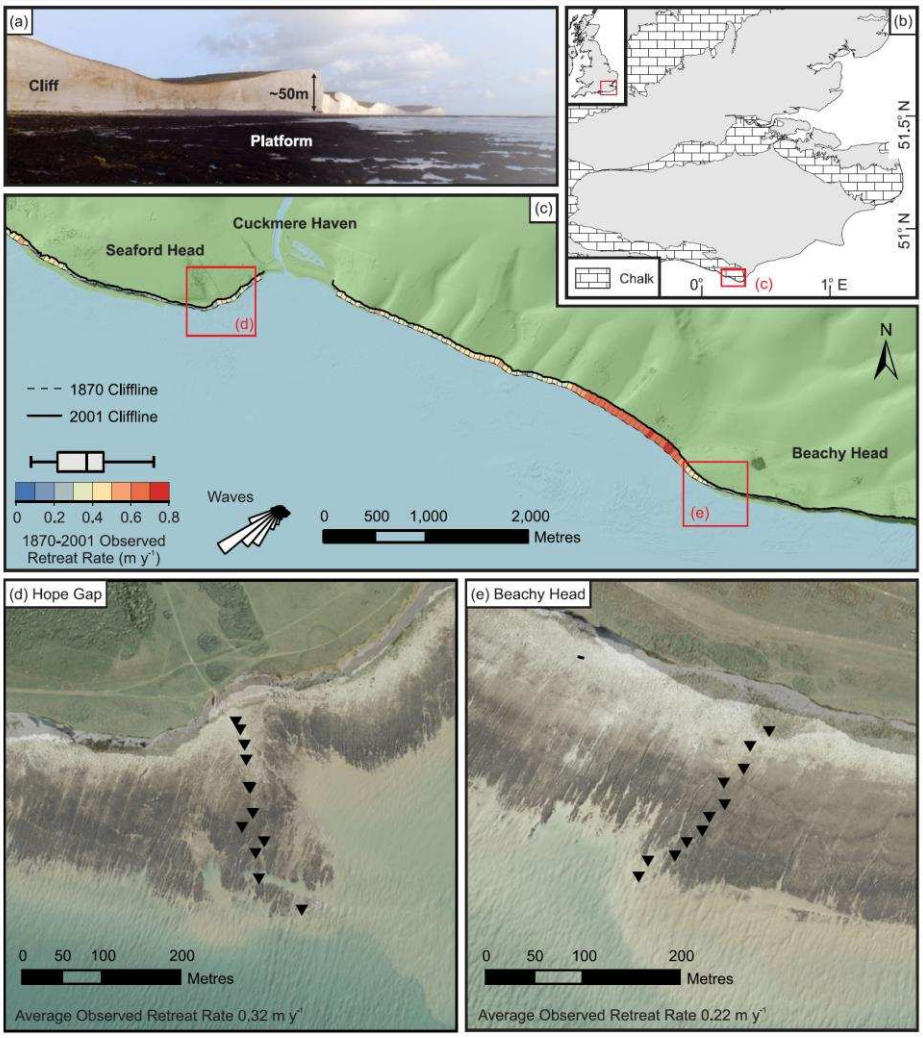

Figure 2: Location and observed historical cliff retreat rates. (a) Photograph of platform and Seven Sisters chalk cliffs. (b) Location map showing study area in Cretaceous Chalk in East Sussex, United Kingdom. (c) Shaded relief map derived from stitched LiDAR topography and multibeam bathymetry (data courtesy of the Channel Coast Observatory (CCO); www.channelcoast.org). Mapped 1870s and 2001 cliff lines and associated observed cliff retreat rates from are plotted along the coast after Dornbusch et al. (7). The box plot shows the 5th, 25th, 50th, 75th and 95th percentile of these historic retreat rates above the legend. The wave rose diagram shows wave conditions during 2014 with dominant wave approach from SW (data courtesy of CCO). (d) and (e) Shaded relief draped with 2008 aerial photographs (data courtesy of CCO) for field sites at (d) Hope Gap and (e) Beachy Head, respectively. Black triangles show the locations of flint samples collected for CRN analysis for use in this study. Average 20th century retreat rates are 0.32 and 0.22 m y^{-1}, respectively.

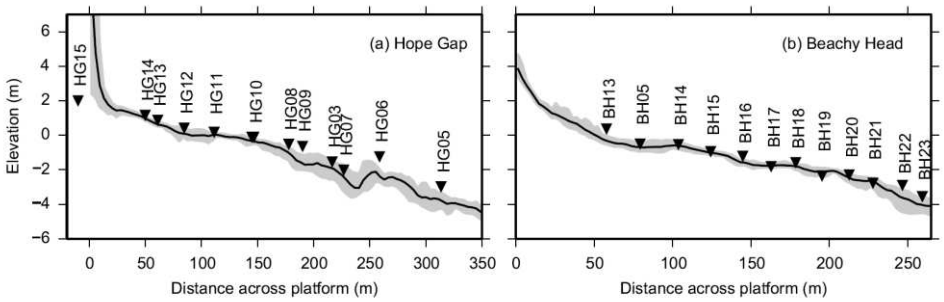

Figure 3: Swath profiles of platform morphology from stitched LiDAR and multibeam elevation data (data courtesy of the Channel Coast Observatory; www.channelcoast.org) and sample locations (black triangles) for (a) Hope Gap and (b) Beachy Head transects. Black lines are mean elevation within a 10 m wide swath, grey shaded region shows the range of elevations within the swath.

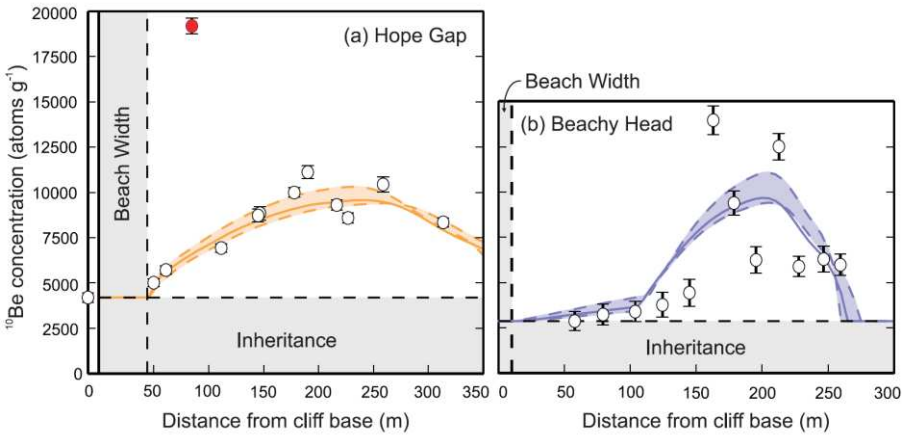

Figure 4: Measured ^{10}Be concentrations and 1σ uncertainties (open circles and whiskers respectively), and most likely retreat scenarios (colored lines and shaded regions showing median and 95% confidence interval) for (a) Hope Gap and (b) Beachy Head transects. Concentrations of ^{10}Be generally increase and then decrease offshore. The sample highlighted in red on the Hope Gap transect (a) was treated as an outlier (see Discussion in text). The minimum measured concentration in each transect was assumed to represent the inherited concentration of ^{10}Be (see text for further discussion). The most likely retreat scenarios in both cases were a recent step change in retreat rate, with (a) a reduction from 5.7 (+0.3/-0.3) to 1.3 (+1.1/-0.3) cm yr^{-1}, 308 (+135/-100) years ago at Hope Gap; and (b) an increase in retreat rate from 2.6 (+0.2/-0.2) to 30.4 (+8.3/-106.) cm yr^{-1}, 293 (+170/-80) years ago at Beachy Head.

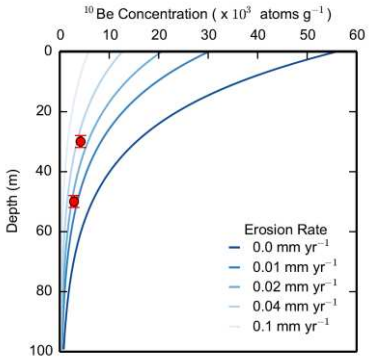

Figure 5: Steady-state ^{10}Be concentrations as a function of depth generated by deep-penetrating muons for surface lowering rates of up to 0.1 mm yr^{-1}. Red symbols show measured inherited concentrations with depth taken as the local cliff height for each site. Measured inheritance is consistent with surface lowering rates of 0.01-0.04 mm yr^{-1}.

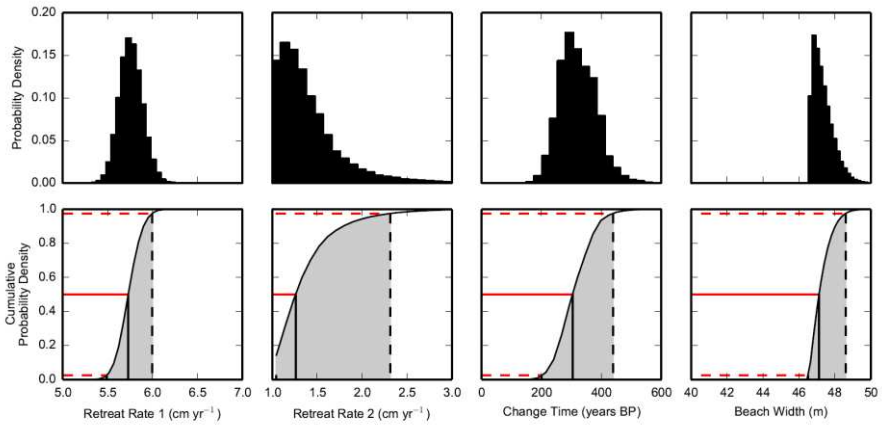

Figure 6: Example probability density (top row) and cumulative probability (bottom row) of the two retreat rates, the timing of change, and beach width for the step-change scenario MCMC ensemble at Hope Gap. Values and uncertainties were taken as the median (solid line) and 95% confidence range (dashed lines and grey shading) from the cumulative density plots on the bottom row.

Supplementary Materials

Table S1 contains data on measured ^{10}Be concentrations conducted for this study. Figures S1-S12 show the MCMC chains of accepted parameter combinations for each retreat scenario, for each transect, and likelihood-weighted histograms for each parameter from which parameter estimates and uncertainties were determined (Table S2-S3). At Hope Gap, similar likelihoods were obtained for the single retreat rate, linear change in retreat rate, and a step change in retreat rate scenarios.

At Beachy Head, a step change in retreat rate performs significantly better than either a constant retreat rate or gradual change in retreat rate. There is a trade-off between ε_2 and t such that a more recent change time coupled to a higher retreat rate produces similar profiles to an older change time and lower recent retreat rate (Fig. S13). Thus, we are unable to constrain whether a more rapid retreat rate initiated more recently, or a slightly slower rate further back in time. As a result of this, there appear to be multiple attractor locations in the parameter space depending on ε_2 and t.

Table S1: ^{10}Be sample and concentration data.

Sample ID	Location (British Nat. Grid)		Distance from Cliff (m)	Elevation above ordinance datum (m)	Mass of quartz dissolved (g)	Mass of carrier added (g)**	Measured $^{10}Be/^{9}Be$ ratio ($\times 10^{-14}$)	± 1σ AMS analytical uncertainty $^{10}Be/^{9}Be$ ratio ($\times 10^{-14}$)	Background-corrected Concentration ^{10}Be ($\times 10^{3}$ atoms g^{-1})***	± 1σ AMS Analytical uncertainty ($\times 10^{3}$ atoms g^{-1})	Inheritance-corrected ^{10}Be** ($\times 10^{3}$ atoms g^{-1})	±**** ($\times 10^{3}$ atoms g^{-1})
	Easting (m)	Northing (m)										
HG-03	551032	97178	216.5	-1.54	65.737	0.973	4.825	0.139	9.31	0.28	5.11	0.39
HG-05	551079	97093	313.5	-2.98	65.862	0.972	4.362	0.124	8.35	0.25	4.15	0.37
HG-06	551025	97133	258.7	-1.24	59.316	0.973	4.881	0.185	10.44	0.42	6.25	0.49
HG-07	551021	97165	226.8	-2.01	64.127	0.974	4.363	0.130	8.59	0.27	4.39	0.38
HG-08	551017	97216	177.8	-0.52	57.464	0.974	4.539	0.115	9.99	0.27	5.80	0.38
HG-09	551004	97198	190.1	-0.64	68.858	0.971	5.995	0.190	11.12	0.37	6.92	0.45
HG-10a	551014	97248	146.6	-0.11	61.812	0.972	4.341	0.176	8.85	0.38	4.65	0.46
HG-10b	551012	97249	144.9	-0.11	56.102	0.972	3.909	0.148	8.73	0.35	4.53	0.44
HG-11	551009	97283	111.3	0.17	53.048	0.971	2.989	0.095	6.93	0.24	2.73	0.36
HG-12	551003	97309	84.6	0.42	50.808	0.971	7.578	0.166	19.19	0.43	14.99	0.51
HG-13	550998	97333	61.0	0.24	56.553	0.970	2.658	0.096	5.71	0.23	1.52	0.35
HG-14	550992	97342	49.8	0.41	50.353	0.971	2.120	0.088	5.01	0.24	0.82	0.36
HG-15*	550906	97384	-5.0	5.0	53.321	0.970	1.905	0.106	4.20	0.27	0	0.38
CFG1405A	-	-	-	-	-	-	0.207	0.130	-	-	-	-
CFG1405B	-	-	-	-	-	-	0.217	0.106	-	-	-	-
BH-05	555919	95501	79.3	-0.50	52.287	0.975	1.901	0.097	3.26	0.57	0.36	0.78
BH-13*	555939	95516	57.8	0.37	61.283	0.973	1.954	0.136	2.87	0.53	0	0.75
BH-14	555913	95477	103.7	-0.53	54.364	0.976	2.015	0.107	3.40	0.56	0.52	0.77
BH-15	555892	95463	124.3	-0.94	41.660	0.974	1.811	0.075	3.77	0.69	0.90	0.87
BH-16	555893	95441	144.8	-1.21	41.172	0.974	2.004	0.114	4.44	0.75	1.57	0.92
BH-17	555877	95427	162.9	-1.81	49.262	0.970	5.828	0.211	13.97	0.78	11.09	0.95
BH-18	555870	95413	178.6	-1.58	45.440	0.972	3.848	0.115	9.39	0.68	6.52	0.86
BH-19	555854	95402	195.4	-2.35	42.785	0.972	2.644	0.121	6.24	0.73	3.37	0.90
BH-20	555842	95388	212.7	-2.29	52.843	0.972	5.617	0.210	12.51	0.73	9.64	0.90
BH-21	555814	95382	227.9	-2.77	52.663	0.971	2.968	0.097	5.88	0.57	3.01	0.77
BH-22	555805	95366	246.7	-2.90	50.237	0.972	3.013	0.180	6.29	0.72	3.42	0.89
BH-23	555813	95349	259.4	-3.55	52.866	0.972	3.014	0.125	5.98	0.60	3.11	0.80
CFG1410A	-	-	-	-	-	-	0.770	0.059	-	-	-	-
CFG1410B	-	-	-	-	-	-	0.485	0.074	-	-	-	-

* Normalized to the 07KNSTD3110 standard with an assumed ratio of 2.85×10^{-12}. Values corrected for chemistry background using average and standard deviation of two full chemistry blanks processed in each batch with errors in sample and blank propagated in quadrature.

** Carrier concentration 204 µg Be g^{-1}.

*** All HG samples were corrected for inheritance with HG-15, which was a fully shielded sample taken from a cave in the cliff. BH samples were corrected for inheritance with BH-05, assuming little accumulation of CRNs.

**** Error propagated as $\sigma_c = \sqrt{{\sigma_a}^2 + {\sigma_b}^2}$ where σ_a is the error of the measured concentration, σ_b is the error of the measured concentration used for the correction (HG-15/BH-05).

Table S2: Results of Monte Carlo simulations for Hope Gap transect

	Retreat Rate Scenario		
Parameters	1. Constant	2. Step Change	3. Linear Change
Retreat Rate 1 (cm yr^{-1})	$5.4\ ^{+0.3}_{-0.3}$	$5.7\ ^{+0.3}_{-0.3}$	$17.8\ ^{+2.8}_{-2.7}$
Retreat Rate 2 (cm yr^{-1})	-	$1.3\ ^{+1.1}_{-0.3}$	$3.7\ ^{+1.0}_{-1.0}$
Change Time (yr BP)	-	$308\ ^{+135}_{-100}$	-
Beach Width (m)	$43.3\ ^{+2.1}_{-1.0}$	$47.0\ ^{+1.6}_{-1.0}$	$40.8\ ^{+4.8}_{-5.6}$
$-\log(L)$	41.1	33.7	40.5

Table S3: Results of Monte Carlo simulations for Beachy Head transect.

	Retreat Rate Scenario		
Parameters	1. Constant	2. Step Change	3. Linear Change
Retreat Rate 1 (cm yr^{-1})	$4.7\ ^{+0.4}_{-0.4}$	$2.6\ ^{+0.2}_{-0.2}$	$1.8\ ^{+1.1}_{-0.8}$
Retreat Rate 2 (cm yr^{-1})	-	$30.4\ ^{+8.3}_{-10.6}$	$6.3\ ^{+0.7}_{-0.8}$
Change Time (yr BP)	-	$293\ ^{+170}_{-80}$	-
Beach Width (m)	$42.7\ ^{+3.0}_{-3.6}$	$17.7\ ^{+3.7}_{-5.5}$	$35.5\ ^{+3.6}_{-4.4}$
$-\log(L)$	121.7	83.7	116.9

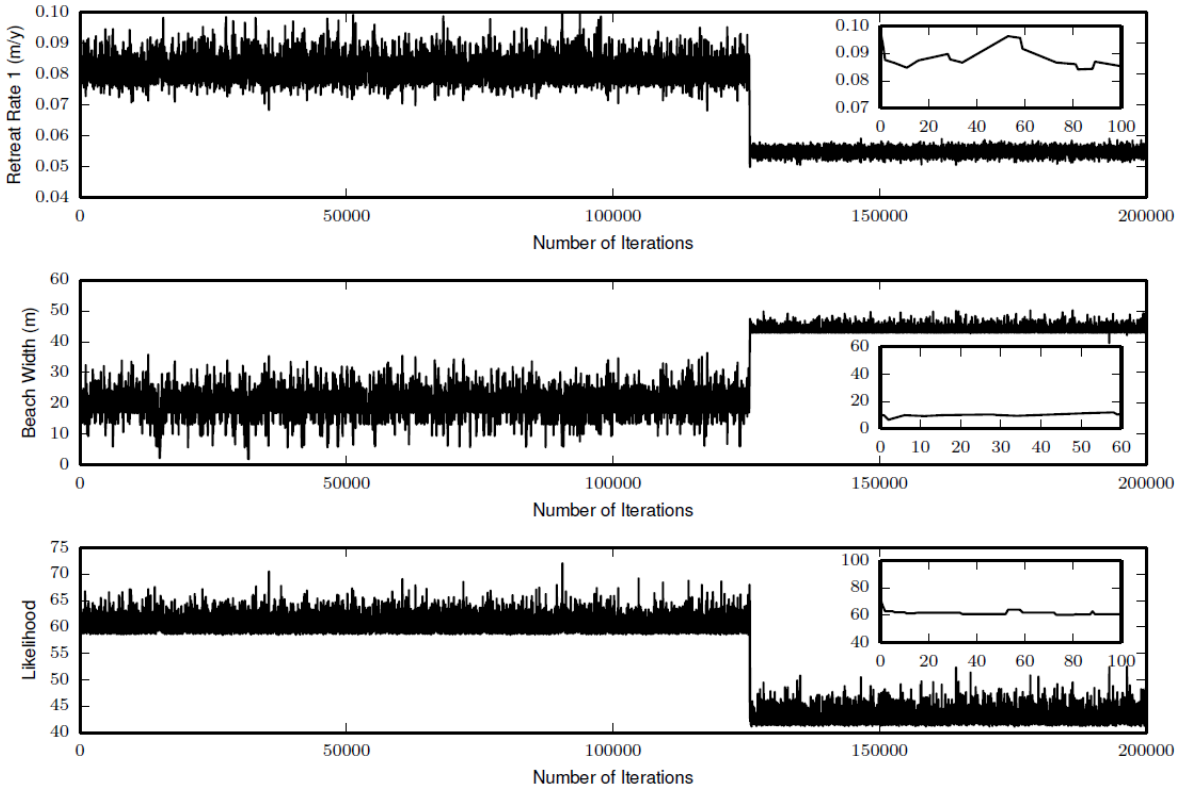

Figure S1: MCMC results for accepted parameters for Hope Gap using a single retreat rate. There were two attractor states in the parameter space with a switch to the more likely state occurring after ~125k iterations in the chain. Inset plots show burn in period.

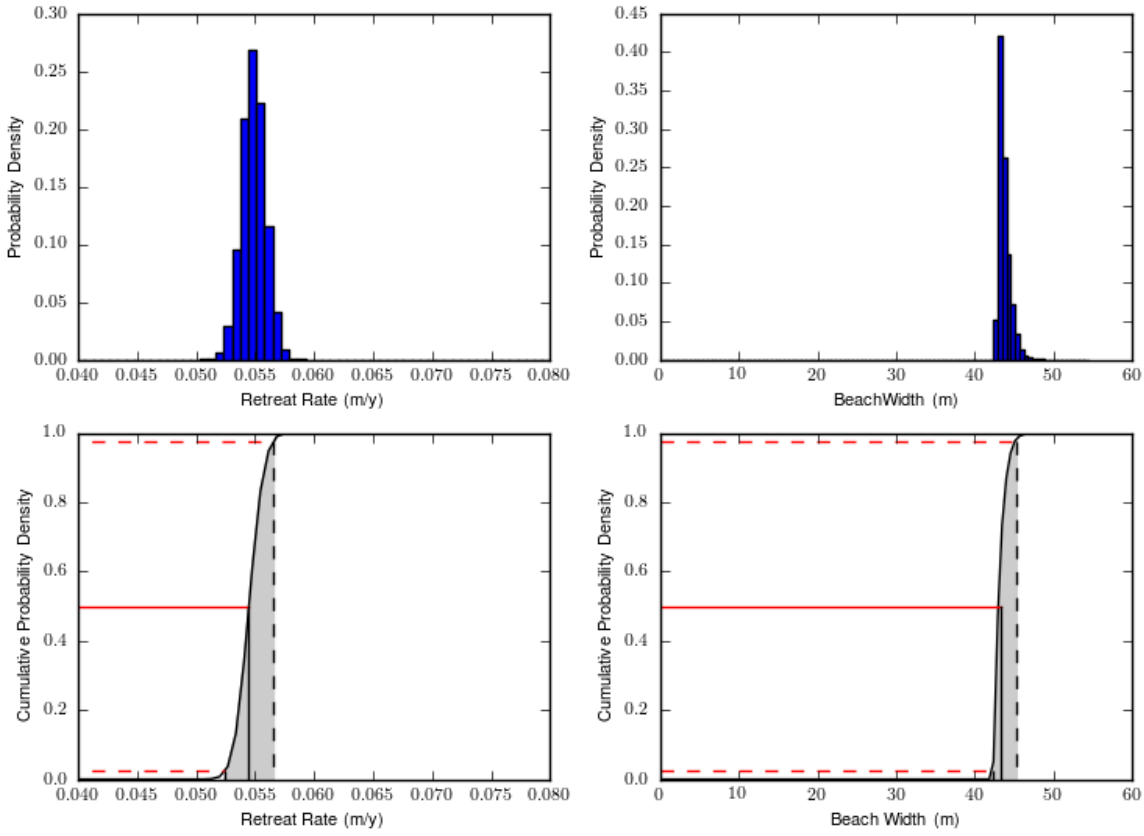

Figure S2: Likelihood weighted histograms giving parameter estimates for Hope Gap from MCMC inversion for single retreat rate scenario. Most likely values taken as the median with 95% confidence intervals. Note these plots include all data from Figure S1.

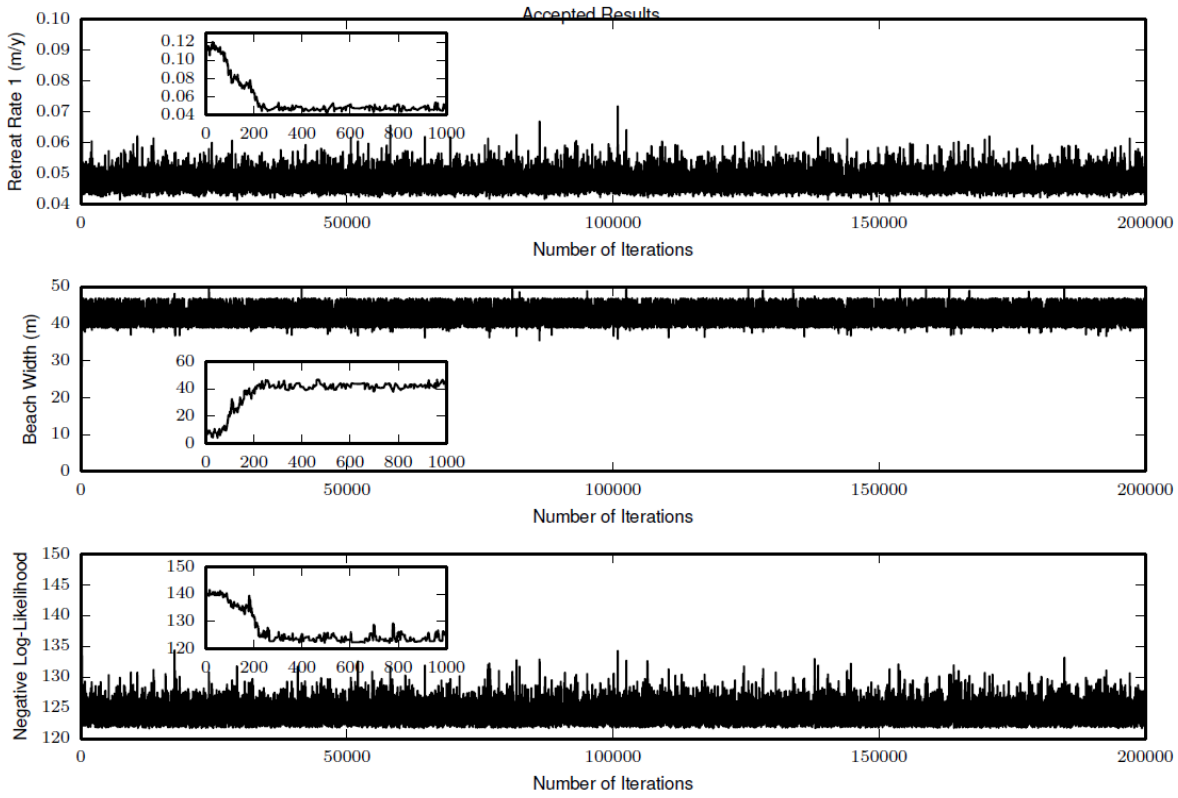

Figure S3: MCMC results for accepted parameters for Beachy Head using a single retreat rate. Inset plots show burn in period.

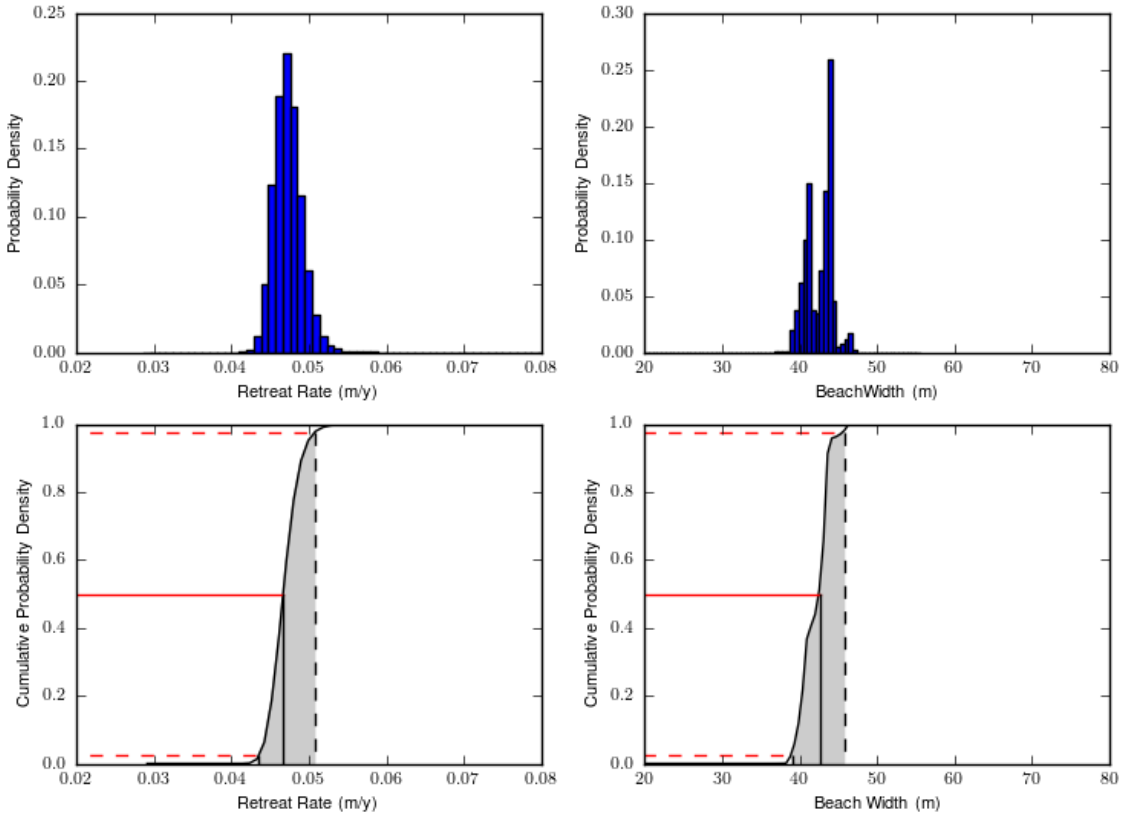

Figure S4: Likelihood weighted histograms giving parameter estimates for Beachy Head from MCMC inversion for single retreat rate scenario. Most likely values taken as the median with 95% confidence intervals. Note these plots include all data from Figure S3.

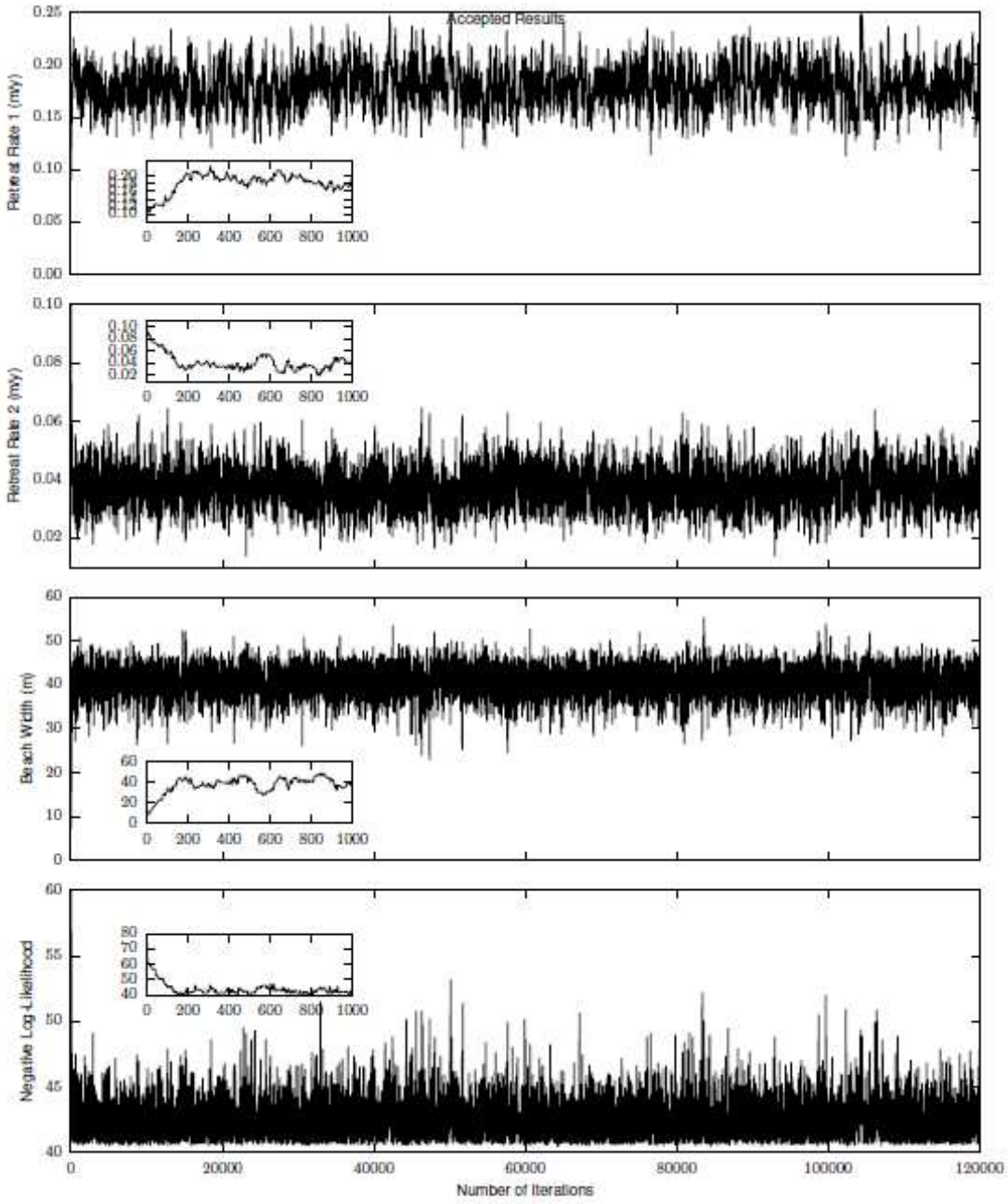

Figure S5: MCMC results for accepted parameters for Hope Gap using a linearly changing retreat rate. Inset plots show burn in period.

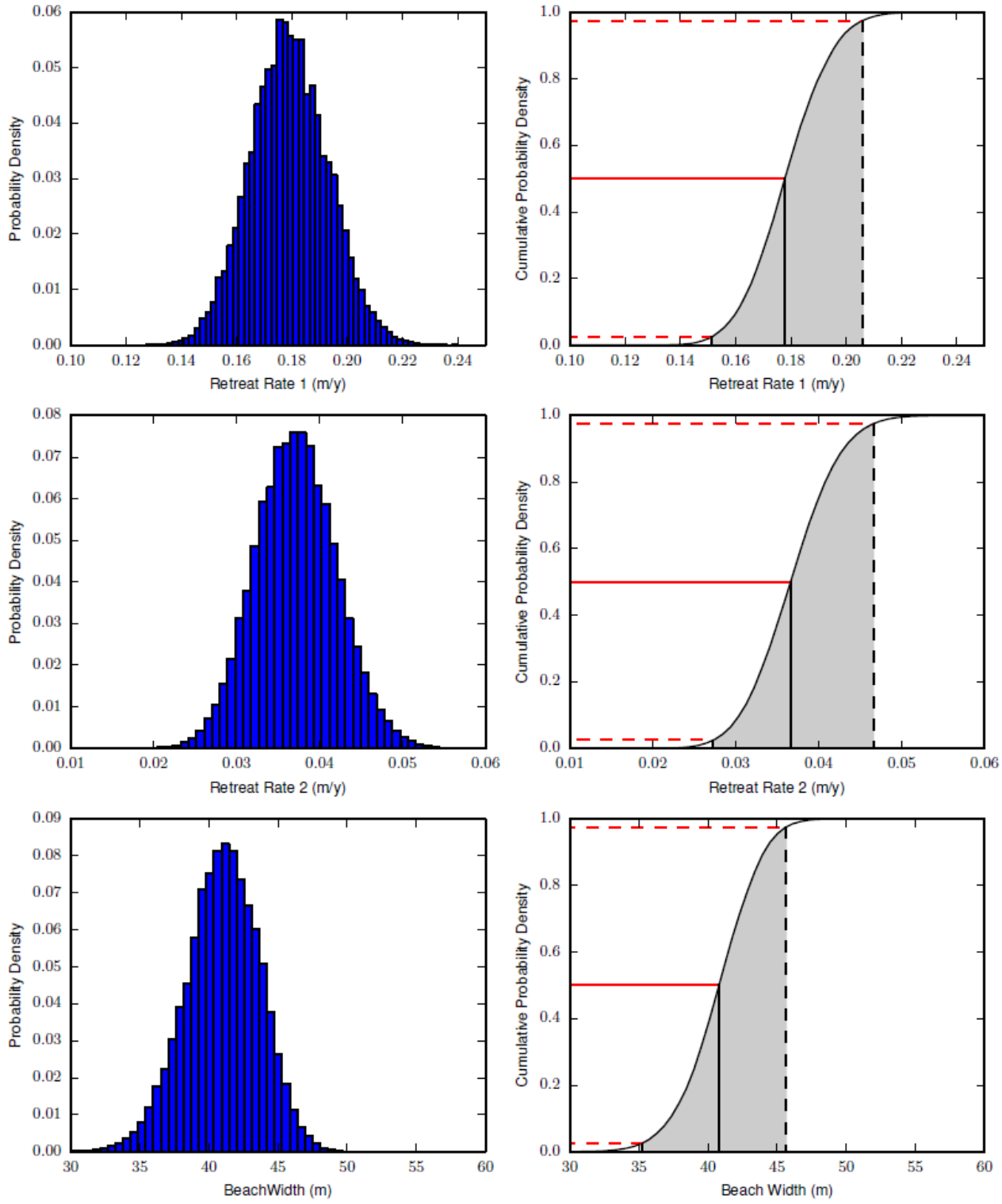

Figure S6: Likelihood weighted histograms giving parameter estimates for Hope Gap from MCMC inversion for linearly changing retreat rate scenario. Most likely values taken as the median with 95% confidence intervals. Note these plots include all data from Figure S5.

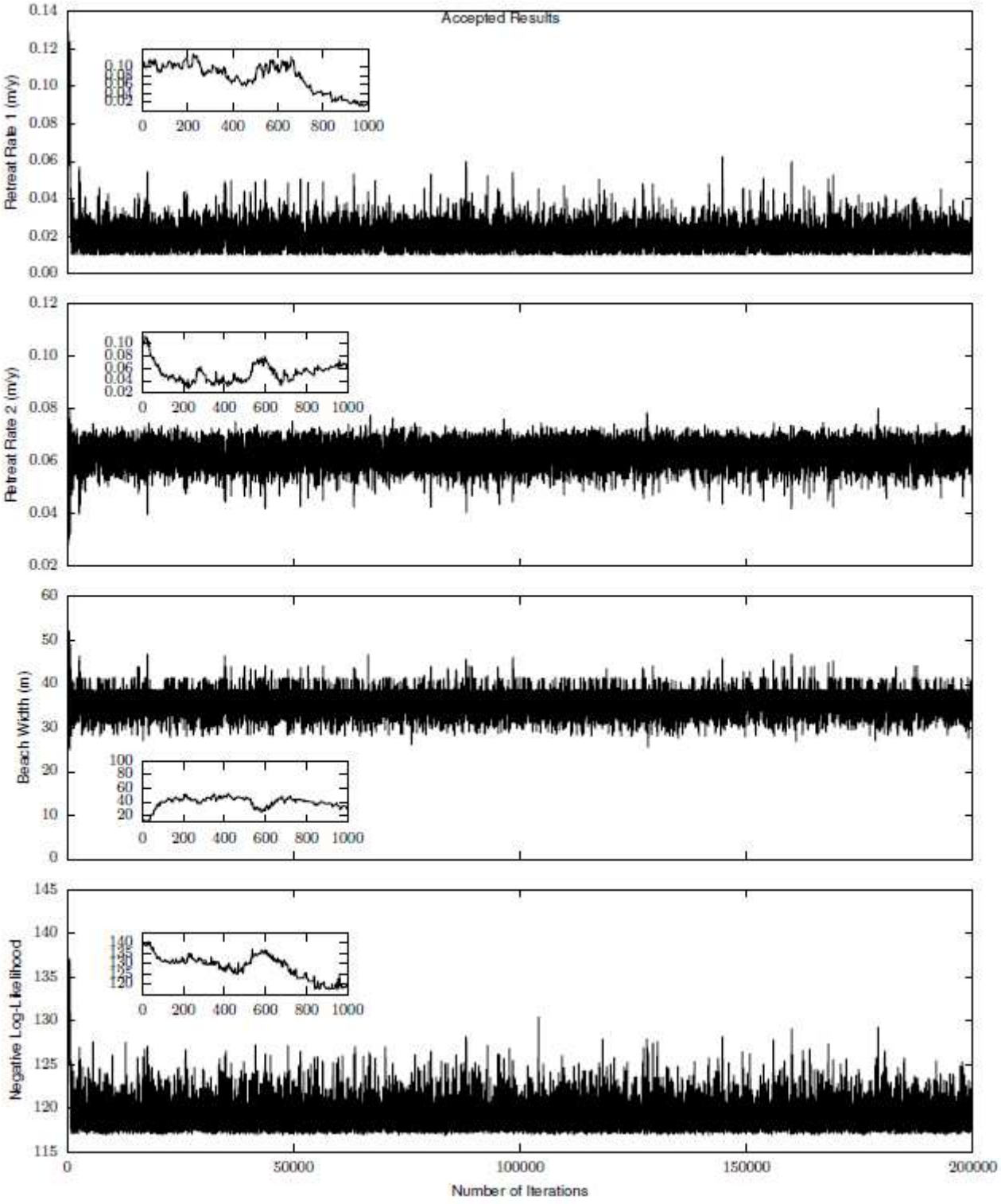

Figure S7: MCMC results for accepted parameters for Beachy Head using a linearly changing retreat rate. Inset plots show burn in period.

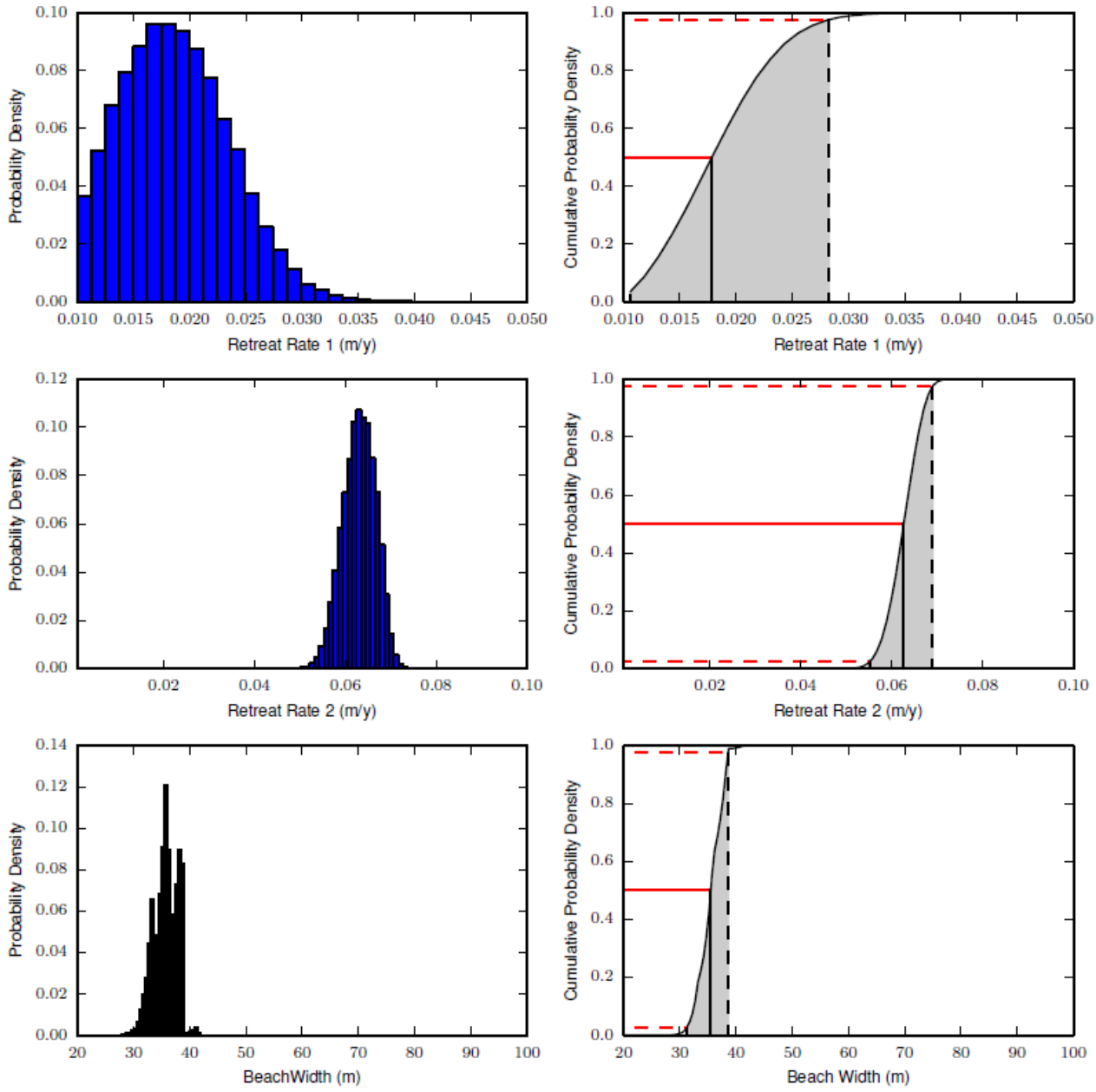

Figure S8: Likelihood weighted histograms giving parameter estimates for Hope Gap from MCMC inversion for linearly changing retreat rate scenario. Most likely values taken as the median with 95% confidence intervals. Note these plots include all data from Figure S7.

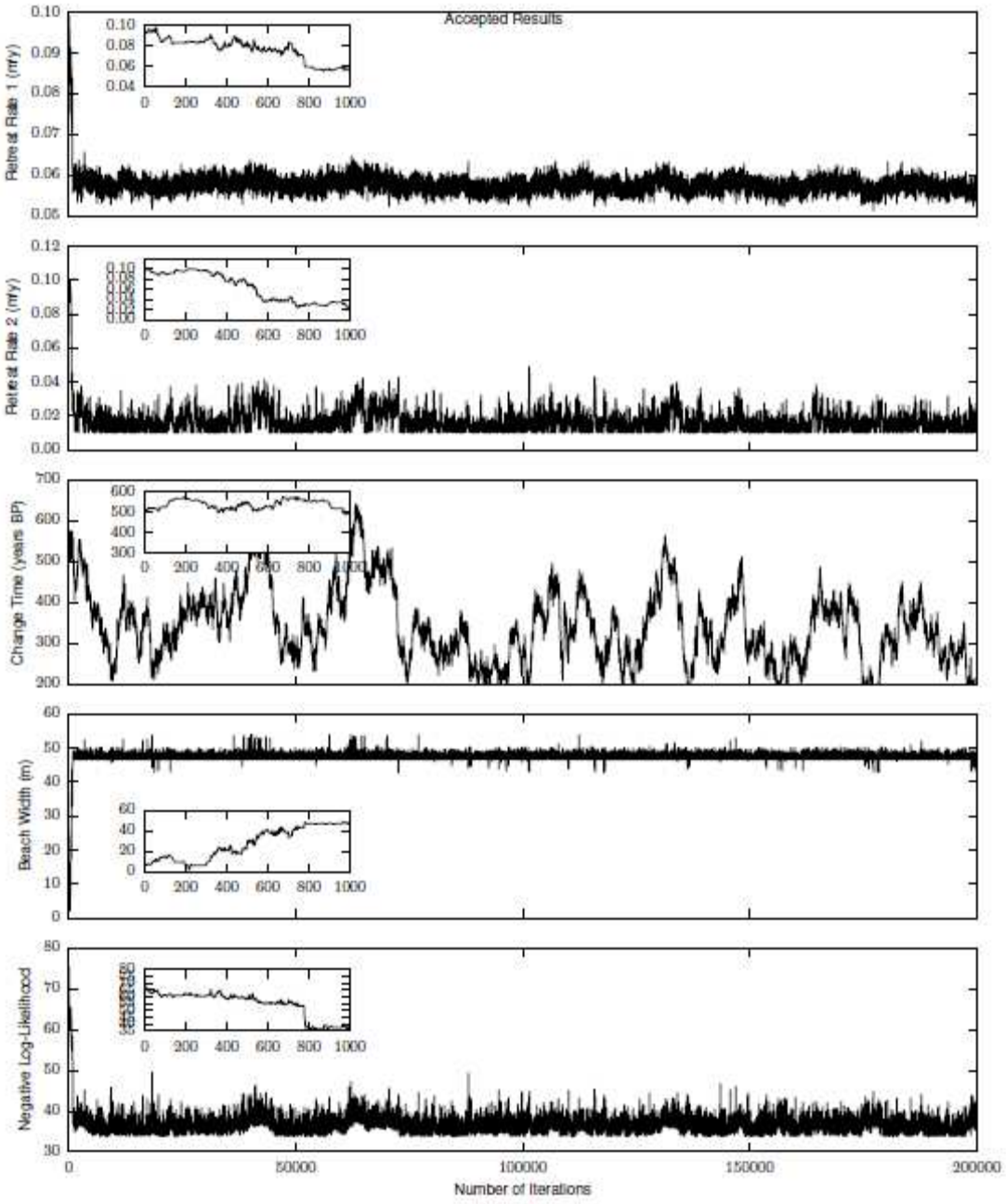

Figure S9: MCMC results for accepted parameters for Hope Gap using a step change retreat rate scenario. Inset plots show burn in period.

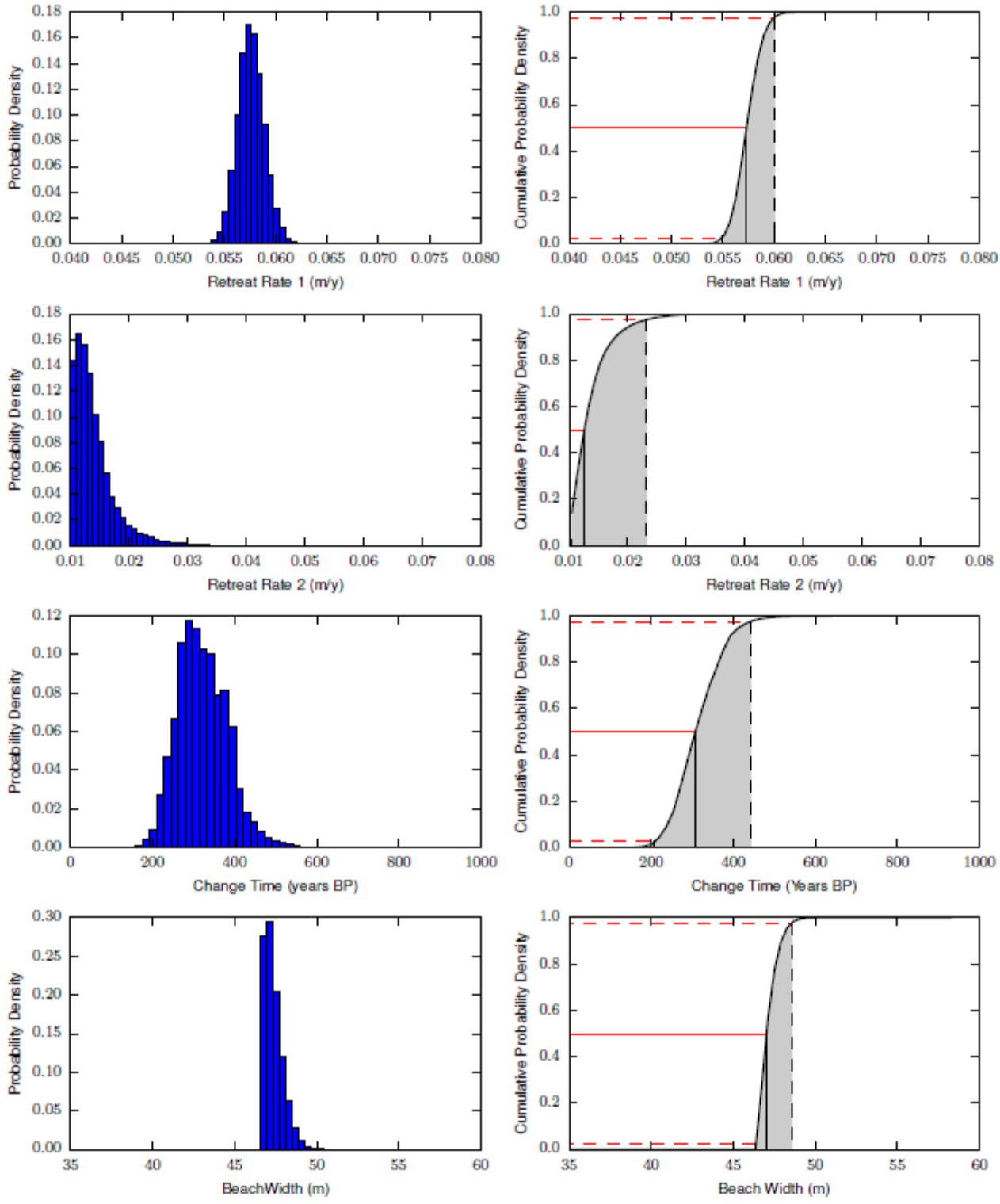

Figure S10: Likelihood weighted histograms giving parameter estimates for Hope Gap from MCMC inversion for a step change retreat rate scenario. Most likely values taken as the median with 95% confidence intervals. Note these plots include all data from Figure S9.

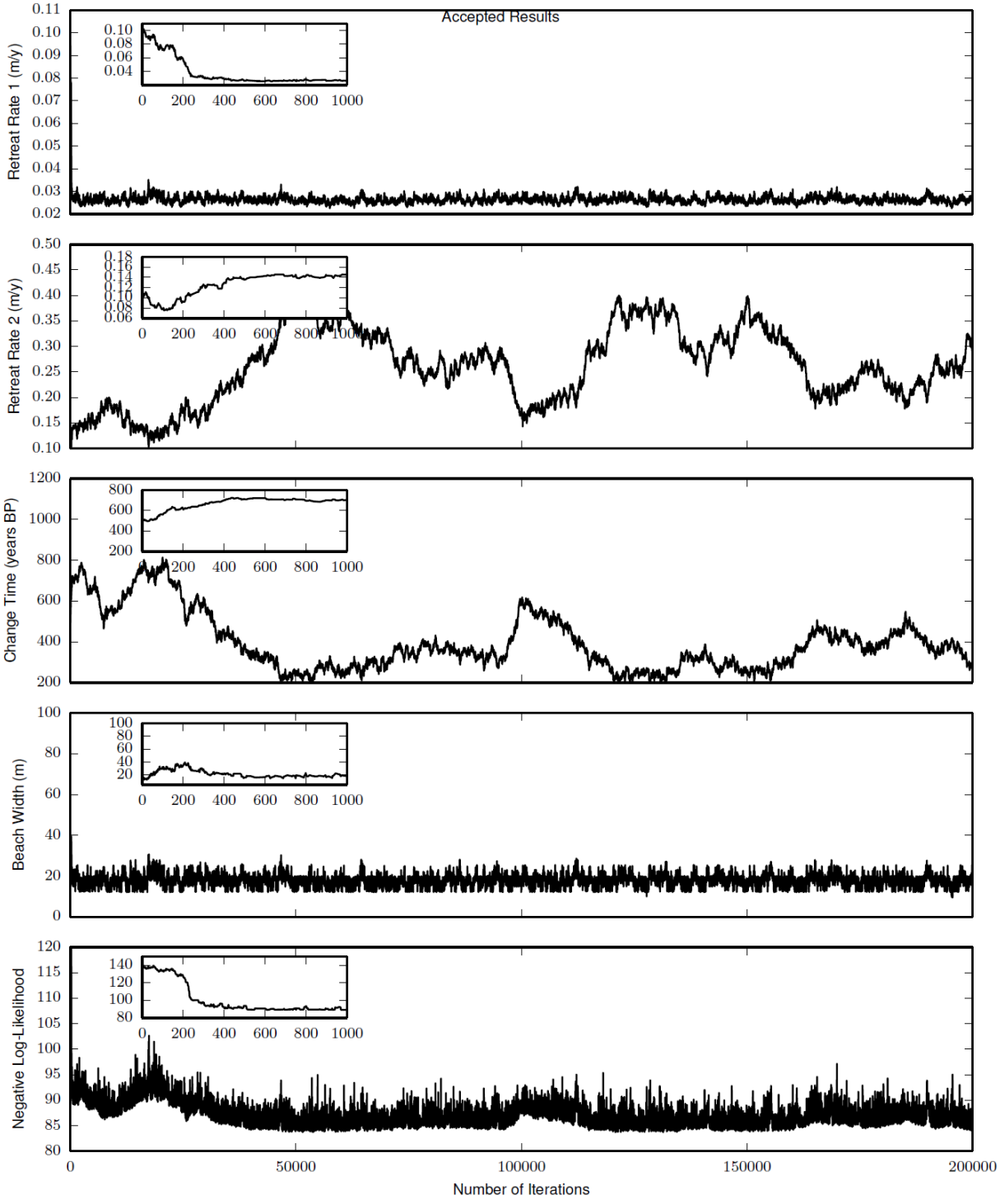

Figure 11: MCMC results for accepted parameters for Beachy Head using a step change retreat rate scenario. Inset plots show burn in period.

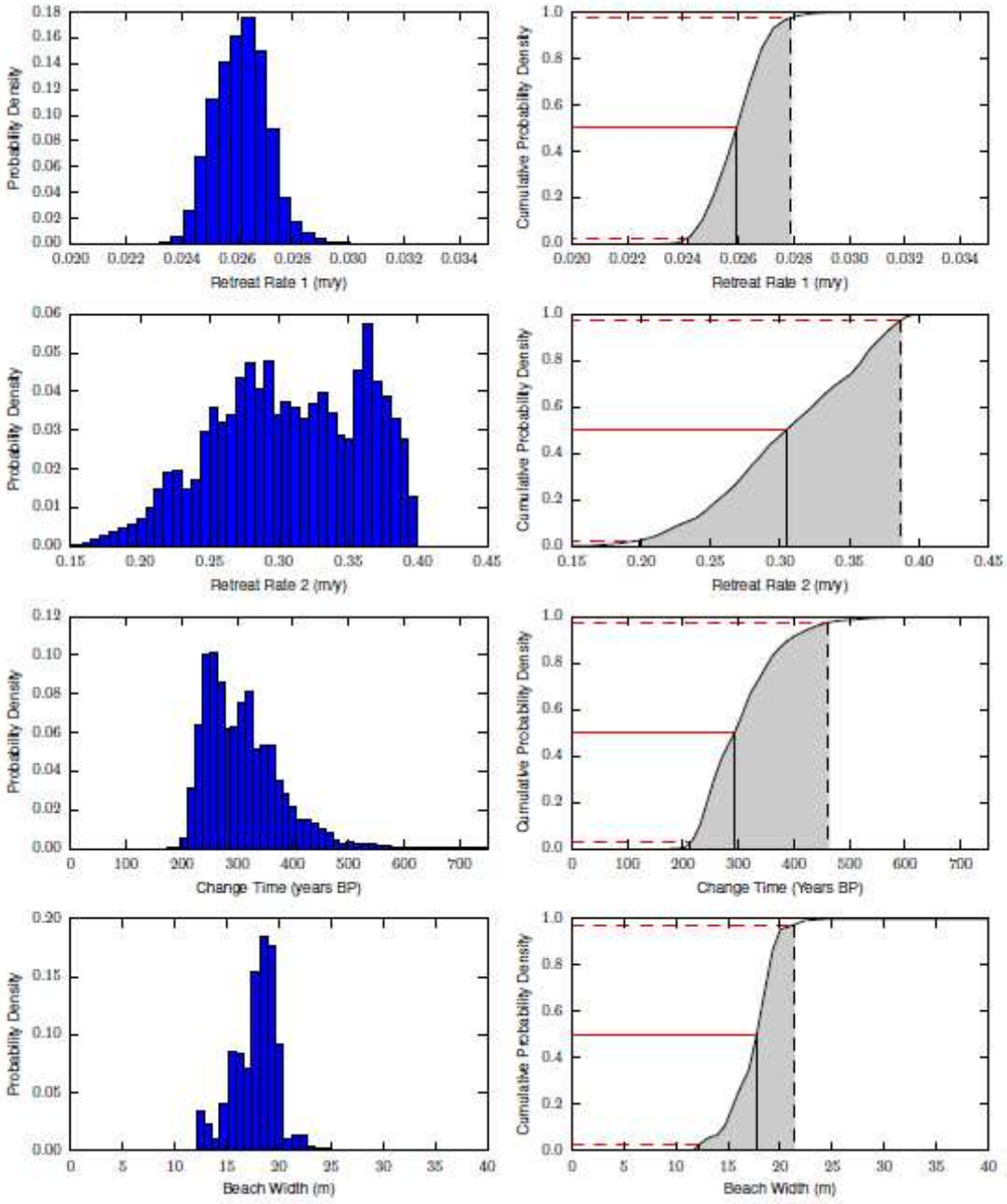

Figure S12: Likelihood weighted histograms giving parameter estimates for Beachy Head from MCMC inversion for a step change retreat rate scenario. Most likely values taken as the median with 95% confidence intervals. Note these plots include all data from Figure S11.

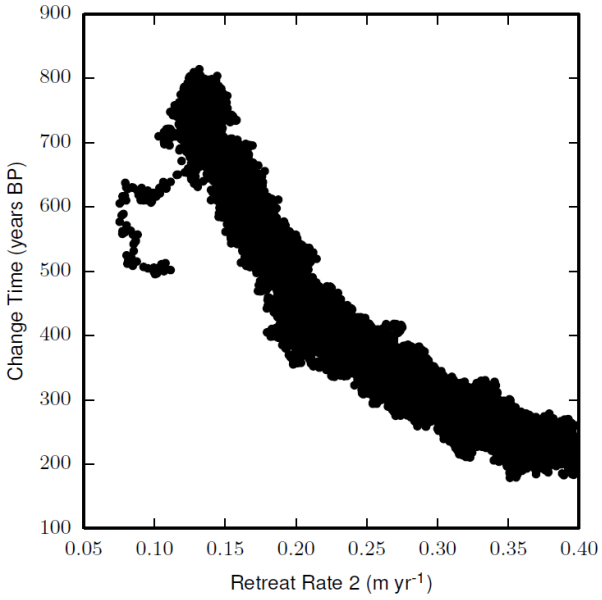

Figure S13: Plot of retreat rate 2 versus the timing of the change between retreat rate 1 and retreat rate 2. Negative correlation reflects trade off between the retreat rate 2 and change time such that a faster recent retreat rate does not need to have occurred as long ago to create the observed distribution of ^{10}Be concentrations.